Shear deformation of nano- and micro-crystalline olivine at seismic slip rates

Manuel Thieme[1], Giacomo Pozzi[2§], Sylvie Demouchy[1*], Nicola De Paola[2], Fabrice Barou[1], Sanae Koizumi[3], Leon Bowen[4]

1 Geosciences Montpellier, CNRS and Université de Montpellier, UMR 5243, 34095 Montpellier, France

2 Department of Earth Sciences, Rock Mechanics Laboratory, Durham University, Durham, DH1 3LE, UK

3 Earthquake Research Institute, University of Tokyo, 1-1-1 Yayoi, Tokyo, Japan

4 Department of Physics, Durham University, Durham, DH1 3LE, UK

§ now at Istituto Nazionale di Geofisica e Vulcanologia Via di Vigna Murata 605, 00143 Roma, Italy

Cite as: Thieme, M., Pozzi, G. Demouchy, S., De Paola, N., Barou, F., Koizumi, S. (2021) Shear deformation of nano- and micro-crystalline olivine at seismic slip rates. Tectonophysics, 802, 228736. https://doi.org/10.1016/j.tecto.2021.228736

* corresponding author
Sylvie Demouchy
Geosciences Montpellier, CNRS
Place Eugène Bataillon, Bat. 22
34095 Montpellier, FRANCE
sylvie.demouchy@umontpellier.fr
+33 (0)467 14 49 42

Abstract

Several thermally activated mechanisms have been proposed to explain the dynamic weakening of faults at fast, seismic slip rates $v > 0.1$ m s^{-1}. Nevertheless, direct constraints from microstructural observations on the operation of such weakening mechanisms are still lacking for most rock forming minerals. This includes olivine, a very refractory mineral relevant for seismic activity occurring in peridotite massifs. Here, we report mechanical data and microstructures of olivine aggregates deformed in a rotary shear apparatus at slip rates from 10^{-2} m s^{-1} to 1 m s^{-1}. A number of 34 shear deformation experiments were performed under axial stresses of 20 MPa and at room temperature. Samples are composed of either synthetic iron-free nanocrystalline forsterite powder (initial grain size = 0.07 μm) or natural iron-bearing olivine powder from San Carlos or San Bernardino (Fo_{91}, Arizona, USA; initial grain size = 70 ± 2 μm). Shear deformation lasts from a few seconds up to 5 minutes and ends after 0.03 to 3 m of slip. Independently of the initial grain size or composition, friction coefficients decrease from peak values of 0.8 to values below 0.4, after only 0.1 m of slip. The recovered samples were characterized by scanning electron microscopy, electron backscatter diffraction and transmission electron microscopy. For all samples, before the onset of dynamic weakening, the deformation localizes in a principal shear zone, well-marked in the natural olivine aggregates by a rapid decrease of grain size down to < 1.7 μm. Variations in texture, fractured grains and the formation of a fine-grained matrix support cataclastic flow at an early stage of deformation, responsible for the foremost grain size reduction. The samples display well-defined zones with partially sintered microstructure, and shape preferred orientation. The initial texture of the cold-pressed starting material is rapidly reduced to a near random distribution after only 0.03 m of slip. All crystal preferred orientations (CPO) remain weak, with a J-index $\lesssim 2$. Based on the microstructures, the dominant deformation mechanism may be enhanced effective diffusion (by surface and grain boundary diffusion) causing mechanical weakening and a viscous behavior, which is then temperature-dependent under sub-solidus conditions. We find no microstructural evidence for frictional melting, flash heating or thermal decomposition. Our results advocate that dynamic weakening of faults is independent of initial grain size, and can be achieved after displacements as low as 0.1 m without production of frictionally induced-melt.

Keywords: olivine, friction, experimental deformation, shear zone, high-velocity torsion

Highlights:

- Deformation of olivine aggregates by torsion at seismic slip rates
- Friction coefficients decrease independently of initial grain size
- Deformation mechanism is thermally activated, and yields to a viscous behavior
- Faults could effectively self-lubricate without an *a priori* presence of weak phases

1 Introduction

Sliding experiments at sub-seismic slip rates (< 1 mm s^{-1}) demonstrated that the friction coefficient μ of most rocks, defined as the ratio of shear stress to normal stress, ranges from 0.6 to 0.85 (Byerlee, 1978). Yet, numerical geodynamic models (e.g. Crameri et al., 2012; Crameri and Tackley, 2015; Nakagawa and Tackley, 2015), seismic stress inversions (e.g., Maerten et al., 2016a, 2016b) and stress inversion combined with slip analyses on natural fault zones (e.g., Bolognesi and Bistacchi, 2018) require significantly lower values of friction coefficients, typically ≤ 0.2, to achieve Earth-like seismic fault behaviors. Additionally, assuming Byerlee-type friction values would cause high shear stresses on faults near the Earth's surface and substantial frictional heat production, and thus melting – which is not observed systematically in the geologic record of active faults (e.g., Saffer et al., 2003; Scholz, 2000, 2002).

Recent studies (e.g., Beeler et al., 1996; Goldsby and Tullis, 2002; Di Toro et al. 2011; De Paola et al., 2015; Pozzi et al., 2018, 2019) have reported experiments using low- to high-velocity rotary shear or deformation apparatuses and the results are questioning whether Byerlee-type friction values are representative of the frictional strength of faults during the propagation of an earthquake. Laboratory experiments approaching seismic slip rates (≥ 0.1 m s^{-1}) report coefficients of friction between 0.1 and 0.3, largely independent of rock types (Di Toro et al., 2004, 2006a, 2006b, 2011; Hirose and Shimamoto, 2005; Han et al., 2007, 2010; Del Gaudio et al., 2009; Mizoguchi et al., 2009; Ferri et al., 2010; Reches and Lockner, 2010; De Paola et al., 2011; Di Toro et al., 2011; Goldsby and Tullis, 2011; Pozzi et al., 2018; Demurtas et al., 2019). These studies have proposed several mechanisms, some being thermally activated, to explain the drastic decrease of the friction coefficient: (1) frictional melting (Hirose and Shimamoto, 2005; Di Toro et al., 2006a; Nielsen et al., 2006); (2) flash heating/weakening (Rice, 2006; Remple and Weaver, 2008; Goldsby and Tullis, 2011; Brantut and Viesca, 2017), (3) the presence of a priori weak mineral phases, such as smectite (e.g., Carpenter et al., 2011), nano powder lubricants (Han et al., 2010; De Paola et al., 2011; Reches and Lockner, 2010) or silica gel lubrication (Di Toro et al., 2004); (4) thermal expansion/pressurization (Rice, 2006; Viesca and Garagash, 2015); (5) phase transformations, i.e. thermally induced decomposition (Di Toro et al., 2004; Han et al., 2007; De Paola et al., 2011; Green et al., 2015); or (6) a mechanism leading to apparent viscous flow (De Paola et al., 2015; Green et al. 2015; Pozzi et al., 2018, 2019). Furthermore, direct microstructural constraints on the operation of such single or combined weakening mechanisms, with the exception of obvious frictional melting (Hirose and Shimamoto, 2005; Di Toro et al., 2006a; Nielsen et al., 2006) are still lacking for most rock forming minerals, including olivine, and a satisfying consensus based on observables has not yet been reached.

Field evidence from the Balmuccia peridotites, pseudotachylites of Cape Corse and the Mt. Maggiore ophiolitic unit (Griggs and Handin, 1960; Obata and Karato, 1995; Andersen and Austrheim, 2006; Andersen et al., 2008; Piccardo et al., 2008), torsion experiments under high normal stress (5 GPa; Bridgman, 1936) and results from theoretical studies (e.g. Ogawa, 1987; Kelemen and Hirth, 2007; Braeck and Podladchikov, 2007; John et al., 2009) all advocate for friction-induced melting in olivine-rich mantle rocks. In addition, the case of the 1994 Bolivia earthquake (magnitude M_w 8.2, at 641 km of depth) has been used to propose that coseismic lubrication occurs by friction-induced melting, based on the estimated low amount of non-radiated energy (Kanamori et al., 1998; Bouchon and Ihmlé, 1999). Nevertheless, to date, the only experimental investigation on peridotites (from Balmuccia) deformed at seismic slip rates (Di Toro et al., 2006b; Del Gaudio et al., 2009) used localized slip between surfaces of two solid natural rock cylinders (at room pressure). The results show frictionally-induced melt, but its rapid generation might have overprinted prior active weakening mechanisms. Moreover, olivine is a valuable testing geomaterial to further decipher the deformation mechanism(s) behind the observed dynamic weakening: How does an initial fine-grained olivine and thus a very refractory and anhydrous material (e.g., high melting temperature) weaken when sheared at seismic slip rates? Does it lead to the same friction coefficient decrease as observed in experimentally deformed natural rocks without (prior) melt generation?

Here, we investigate the dynamic weakening occurring in cold-pressed powder of monomineralic olivine when sheared at seismic slip rates (under lower normal stresses than expected at depths relevant for uppermost mantle rocks) and before the generation of melt. We also test dry olivine with different compositions (Fo_{91} and Fo_{100}) as the presence of iron was previously identified as a weakening agent in olivine (e.g., in axial compression experiments by Zhao et al., 2009; and in Vickers indentation tests by Koizumi et al., 2020), and with two different initial grain sizes (micrometric and nanometric), which could be applicable to gouges in ultramafic rocks (e.g., prior to formation of serpentinized peridotites, Swiatloski et al. 2018; Strating and Vissers, 1994).

The subsequent microstructural investigation comprises scanning electron microscopy, electron backscatter diffraction and transmission electron microscopy. Afterward, we discuss our results to further decipher the potential weakening mechanisms which could operate at seismic conditions in olivine aggregates, in the context of the previously proposed deformation mechanisms.

2 Materials and methods

2.1 Starting material

We used three types of dry $(Mg,Fe)_2SiO_4$ olivine starting material with different iron contents of Fo_{91} and Fo_{100} (i.e., $Fo_{\%}$: 100 × Mg/(Mg+Fe)): (1) Iron-free nanocrystalline olivine powder with an average grain size of ϕ = 0.07 μm, synthetized by Koizumi et al. (2010). The mineral powder was prepared through solid state reaction of high purity source powders and synthesized at 960 °C for 3h in atmospheric condition. Hereafter, we refer to this starting material as 'nanoFo_{100}'. (2) Powder from crushed iron-bearing olivine from San Carlos (Arizona, USA) with a composition close to Fo_{91} (see Buening and Buseck, 1973; Frey and

Prinz, 1978) referred to in the main text as ‘SC olivine’. (3) Powder from crushed iron-bearing olivine from the San Bernardino volcanic field, also located in Arizona, USA (Lynch, 1978; Neville et al., 1985). This material is referred to in the main text as ‘SB olivine’. Contrary to SC olivine, SB olivine is not commonly used for deformation experiments, thus the composition of SB olivine was tested by quantitative energy dispersive spectroscopy (EDS) as approximately $Fo_{90.7}$ (see details in Figure S1 and Table S1), which yields a composition almost identical to San Carlos olivine ($Fo_{91.0}$).

SC and SB olivine powders were both prepared by hand-picking optically inclusion-free single crystals and manually crushing them with an agate mortar and pestle. Crushed grains were dry sieved and only the grain fraction between 63 – 90 μm (70 ± 2 μm in average) was used for deformation experiments. San Carlos olivine has a naturally extremely low hydrogen concentration of less than 1 ppm wt H_2O (e.g. Mackwell et al., 1985; Demouchy, 2010), ruling out *a priori* a potential water weakening effect (e.g. Mackwell et al., 1985; Mei and Kohlstedt, 2000; Demouchy et al., 2012; Tielke et al., 2017). Potential hydrogen incorporated in the $NanoFo_{100}$ starting materials was removed during powder synthesis at high temperature (Koizumi et al. 2010; analyzed by gas chromatography-mass spectrometry), reducing hydrogen concentration to undetectable level as confirmed recently by Fei et al. (2018).

2.2 Deformation assembly and apparatus

A total number of 34 experiments were performed with a low- to high-velocity rotary (LHVR) shear apparatus at the Rock Mechanics Laboratory, Durham University (UK; Model MIS-233-1-77; e.g., Ma et al. 2014, De Paola et al. 2015, Pozzi et al. 2018). Unconsolidated olivine powders were cold-pressed into a hollow cylinder (annular chamber) by two pistons and confined using an external ring (25 mm diameter) and inner cylinder (10.5 mm diameter) made of polytetrafluoroethylene (PTFE) as shown in Figure 1. The pistons are titanium alloy cylinders with 0.5 mm deep machined pyramidal grooves to produce roughness at the contact interface between the cylinder and the simulated gouges (Figure 1a). To prevent significant powder extrusion during the experiment, the PTFE ring was tightened to the lower titanium cylinders with a hose clip (Figure 1b). The inner edges of the PTFE cylinder were machined and smoothed to reduce ablation and contamination of the sample. The pistons are mounted to the top (dynamic) and bottom (static) shaft of the apparatus, where two hydraulic mechanical locks maintain the alignment of the assembly during experiments. All experiments were run at room temperature and humidity. One gram of SC and SB olivine powder was used per experiment resulting in a layer of approximately 1.2 mm of thickness before compression. The nanoFo_{100} powder is less dense due to electrostatic repulsion between the nano-particles. Hence, only 0.7 g of nanoFo_{100} was used per experiment. This amount still resulted in a layer thickness of approximately 5.1 mm before compression.

Before torsion, the powders were cold-pressed *in situ* by applying 20 MPa of normal (axial) stress (constant load of 8.09 kN), applied for at least one minute. This step generates an initial sample thickness of 800 μm for SC or SB olivine and 1000 μm for nanoFo_{100}, excluding the 500 μm groove depth above and below the sample (Fig. 1a). The normal stress is maintained constant during deformation, but there is no confining medium being used in this apparatus. Target slip velocities were 1 m s^{-1}, 0.1 m s^{-1} and 0.01 m s^{-1} at the reference radius (defined as r_r = (external radius + internal radius) / 2 = 8.9 mm). Experiments were stopped at predefined values of slip - and hence at different stages in the mechanical curves - to provide sample microstructure development during the transient evolution of friction from peak values in Byerlee's range to quasi steady state values (e.g., samples 1011, 1012, 1008, 1010). Theoretically, this allows the investigation of the deformation mechanisms and their impact on frictional strength evolution.

The acceleration and deceleration of the deformation cylinders were controlled by a signal generator (NF corporation DF1906), to obtain constant velocity throughout the experiment. Due to the apparatus acceleration, the maximum target slip rate of 1 m s^{-1} was reached in 260 ms and 200 μm of slip, giving an acceleration velocity of 3.85 m s^{-2}. Sampling frequency ranged between 500 Hz and 5 kHz depending on slip rate. The torque is measured on the bottom shaft by two compression load cells with a resolution of ± 5×10^{-4} kN. Axial displacement is measured by a high sensitivity strain gauge with a resolution of ± 2×10^{-3} mm. Axial load cell resolution is ± 5 N. The applied load (and normal stress) is kept to target by a high-precision air regulator. Since the slip velocity v in the sample depends on the radius r, we calculate an equivalent slip velocity v_e at the reference radius (r_r = 8.9 mm) as

$$v_e = 2\,\pi\; r_r\; R \qquad \text{eq. (1)}$$

where R is the revolution rate of the titanium pistons holding the olivine aggregate. Likewise, we calculate an equivalent slip d_e at the reference radius as

$$d_e = v_e\, t \qquad \text{eq. (2)}$$

where t is time (that is the duration of the deformation experiment). To be consistent with the calculated values of v_e and d_e, once we successfully extract chips of the deformed aggregates (Fig. 1c), all our thin sections are cut or polished down perpendicular to the shear plane at the reference radius (Fig. 1d and 1e). The average shear strain γ has been calculated as

$$\gamma = \tan\varphi = \frac{r_r\theta}{2h} \qquad \text{eq. (3)}$$

where φ is the angular shear, θ is the angular displacement in radians and h is the average slip zone thickness inferred from scanning electron microscopy (SEM) imaging (i.e., 30 μm). The average thickness of the slip zones satisfies the condition $h \leq 4\sqrt{\kappa d/v}$, where κ is the thermal diffusivity and d the slip, which allows to treat the slip zone as a zero-thickness plane.

The temperature of the sample could not be measured directly, due to the geometry of the deformation assembly and the apparatus, which prevents the insertion of a thermocouple in direct or close contact with the sample. Additionally, temperature record would be extremely challenging due to high temperature gradients and short timescales of the experiments (i.e., few seconds up to 5 min). Nevertheless, the temperature evolution along the principal shear zone

(PSZ) during deformation can be estimated based on frictional heating, heat capacity and thermal diffusivity of olivine, following Rice's (2006) approach,

$$\Delta T = \frac{\mu\sigma_n\sqrt{vd}}{\rho c_p\sqrt{\pi\kappa}} \qquad \text{eq. (4)}$$

where μ is the measured instantaneous friction coefficient, σ_n the normal stress (20 MPa), ρ the sample density and c_p the specific heat capacity. The temperature, density, thermal diffusivity, specific heat capacity, and also silicon (Si) self-diffusion diffusivity and silicon diffusive characteristic distance are calculated iteratively for each data point, as following:

- Density is calculated using the thermal expansion coefficients of Fei (1995) and ρ_0 = 3371.2 kg m^{-3} of Zhang and Bass (2016) as

$$\rho = \rho_0 \left(1 - \left(3.304\times10^{-5} + 0.742\times10^{-8}\ \mathrm{T} - 0.538\ \mathrm{T}^{-2}\right)\mathrm{T}\right). \qquad \text{eq. (5)}$$

- Thermal diffusivity is calculated using values from Xu et al. (2004) as

$$\kappa = 1.1135\ (298/\mathrm{T})^{0.563}. \qquad \text{eq. (6)}$$

- Heat capacity following Sun et al. (2018) as

$$c_p = 1585 - 1.23\times10^{4}\ \mathrm{T}^{-0.5} - 3.13\times10^{6}\ \mathrm{T}^{-2} - 3.18\ \mathrm{P} + 8.41\times10^{-2}\ \mathrm{P}^{2}. \qquad \text{eq. (7)}$$

- Grain growth equations can be used as a proxy for grain boundaries (GB) and surface diffusion coefficients of Si in olivine. We used results from growth experiments on monomineralic aggregates of dry forsterite from Karato (1989) yielding

$$D_{Si}^{GB+Surface} = 1.6\times10^{-8}\exp\left(-160\ \mathrm{kJ/RT}\right), \qquad \text{eq. (8)}$$

where R is the gas constant and T the absolute temperature in K. Furthermore, characteristic distances of Si diffusion in dry forsterite (reported in Table 1) can be estimated as

$$L_{Diff} = 2\sqrt{\textstyle\sum_0^t D_{Si}^{Surface}\,dt}\ , \qquad \text{eq. (9)}$$

where dt is the time step given by the sampling frequency. Additionally, L^*_{Diff} was also calculated for the maximal calculated temperature and for the total duration of the considered experiment to further estimate the impact of the gradual temperature increase on finite diffusive characteristic distances (Table 1).

2.3. Electron microscopy and electron backscatter diffraction

Starting material powders, cold-pressed undeformed powder and sheared samples were analyzed using a FEI Quanta 200 FEG SEM at the Microscopy Platform of Montpellier University (France) and a FEI Helios Dual Beam Nanolab 600 FEG SEM at the Department of Earth Sciences Durham (Durham University, UK). Microstructure analyses using electron backscatter diffraction (EBSD) were performed at Geosciences Montpellier (Montpellier University, France) with a CamScan X500FE CrystalProbe. Transmission electron microscopy was performed using a JEOL 2100F FEG at the Department of Physics Durham (Durham University, UK).

Post-deformation samples display Riedel fractures and thermal cooling cracks, making samples very fragile and their recovery very challenging (Fig. S2). Considering that removal of deformed samples from the sample assembly usually results in the sample breaking (Fig. 1c), chips of deformed samples were carefully removed with tweezers. Resulting sample chips were mounted in cyanoacrylate with the shear plane aligned vertically (Fig. 1d) and embedded in epoxy. Epoxy mounts were polished to reveal a cross section through the sample at the reference radius used in eq. (1) and (2) (Fig.1e). Polishing included a final chemo-mechanical step using colloidal silica with 0.04 μm particles, and an average polishing duration of 0.2 – 4 h. Exposed sample surfaces were then carbon coated with a coating thickness of 10 – 20 nm for SEM images. For EBSD analyses, only the zone surrounding the area of interest was carbon coated, to preserve Kikuchi pattern clarity and indexing quality. Additionally, a copper-carbon tape was applied on the edges of the epoxy plug to improve conductive connection to the EBSD sample holder.

EBSD data were acquired with the Oxford instruments HKL Aztec2 software and treated with the MTEX toolbox (Hielscher and Schaeben, 2008; Bachmann et al., 2010). EBSD maps were obtained with an acceleration voltage of 17 kV, a beam current of 10 nA, a working distance of 25.0 mm and an exposure time of 28.8 ms. Acquired mineral phases were olivine, diopside, enstatite and chromite. Step size of EBSD maps ranges from 0.2 to 2 μm. While SC and SB olivine samples were successfully prepared for EBSD mapping, nanoFo_{100} samples were extremely difficult to analyze due to a lack of competent sintering. The small grain size in combination with pores and open grain boundaries result in extreme electrostatic charging and poor indexation by EBSD as illustrated by Figure 2b (see also Figure S3). EBSD data treatment involved removal of wild spikes and replacement of non-indexed pixels with neighboring values where 7 neighbors with identical orientations were present. Grain boundaries were defined by a misorientation to the next pixel higher than 10°. Grains containing less than 15 indexed pixels were rejected. The density of the orientation distribution function was calculated using an axially symmetric de la Vallee Poussin kernel, with a half-width of 10° (band-width of 28 in spherical harmonic coefficients). The J-index, which is a measurement of the texture strength (Bunge, 1982), was calculated as the integral of the square of the orientation distribution function. Additionally, we calculated statistical parameters such as the percentile average relative indented surface (PARIS, a shape parameter that measures the convexity of a grain) and the kernel average misorientation (KAM, which is a measure of local grain misorientation), the latter being considered as a suitable proxy for dislocation density (*e.g.*, Wallis et al., 2016).

For transmission electron microscopy (TEM), a section of sample 1095 was cut perpendicular to the PSZ with a focused ion beam (FIB) using a Helios Dual Beam Nanolab 600 scanning electron microscope at the Department of Physics, Durham (Durham, UK). TEM images on the JEOL 2100F FEG were obtained in scanning mode (S-TEM) in both bright field and high-resolution electron microscopy (HR-TEM).

3 Results

Out of 34 deformation experiments, 28 showed reproducible mechanical data, which are summarized in Table 1. Additionally, two experiments have been performed to record the cold-press stage of the nanoforsterite and olivine powder (runs 1013 and 1009). The SEM characterization of the initial powder and microstructure after the *in situ* cold-press step are shown in Figure 2. Since no sintering under high pressure and high temperature was performed, the cold-pressed samples present an expected high level of porosity (> 30 %) and internal cracks. Nevertheless, the exact porosity is difficult to evaluate due to significant pluck out during sample preparation and polishing (also illustrated in Figure S4).

3.1 Mechanical data and temperature estimates

Mechanical curves of all deformation experiments are shown in Figure 3. For a large majority of the samples, the evolution of the friction coefficient as a function of displacement shows four distinct stages: (I) a steep increase up to $\mu = 0.6 – 0.7$ upon acceleration to target velocity; (II) strain hardening stage with friction slowly increasing to maximum values of 0.85, attained when reaching the target velocity; (III) transient stage characterized by an initial rapid decrease of friction, followed by a decrease of friction at a lower rate toward almost constant μ at ~ 0.3, attained for experiments performed at 1 m s^{-1}, and at $\mu \sim 0.5$ for experiments performed at 0.01 m s^{-1}; and a final (IV) re-strengthening stage upon deceleration and hence cooling for samples deformed at 1 m s^{-1} or 0.47 m s^{-1}. Note that the low-frequency signal in Figure 3b is typical for the high velocity frictional testing apparatus and arises from cyclic elastic oscillation of the column due to small misalignments of the sample assembly (e.g., Di Toro et al., 2006b; Smith et al., 2015).

The friction coefficient stabilizes after a certain amount of slip (> 0.3 m, stage III), and one could argue that the system enters a quasi-steady state regime. Unlike conditions in low strain torsion experiments, in the high strain experiments presented here temperature spontaneously increases due to frictional heating, which scales with slip; hence, the friction coefficient never becomes truly independent of the amount of slip. It will also be sensitive to temperature variation and stress localization variation (e.g., change of PSZ loci). Thus, we refer to this stabilization of the friction coefficient as 'quasi steady state' for a given velocity.

During stage III, experiments performed at slip rates of 1 m s^{-1} generally yield lower coefficients of friction than experiments deformed at 10^{-2} m s^{-1} for given values of displacement. The SC and SB olivine samples (grain size: 70 ± 2 µm) yield similar friction coefficients as nanoFo_{100} (grain size: 0.07 µm). Deformation at intermediate slip rates of 0.1 m s^{-1} unfortunately resulted in significant extrusion of powder during stage III, which is likely to have caused the observed abnormal continuous drop of the friction coefficient (Fig. 3d). As no quasi steady-state conditions were reached in these experiments (samples 972, 995 – 999, and to some extend 1000 and 1006), the mechanical results of these experiments are dubious and we preferred not to treat them further.

For SC olivine, we repeat the same experiment five times, but stop at increasing values of slip (Table 1, Fig. 3c, sample 1011 at 0.03 m; sample 1012 at 0.07 m; 1008 at 0.12 m; 1010 at 0.58 m and 1007 at 0.97 m). This series demonstrates the reproducibility of the friction coefficient evolution for these torsion conditions. Furthermore, all quasi steady state values of friction are compiled in Figure 4 (average is 0.27 ± 0.3 at at 1 m s^{-1}). Here, the minimal, maximal and average friction coefficient and its standard deviation are compiled for olivine and nanoFo_{100} after 0.4 to 1.4 m of slip. Based on the best quasi steady-state curves (lowest standard deviation experiments: 990, 1007 and 1003), the average friction coefficient is equal to 0.26 ± 0.01 at 1 m s^{-1} (Fig. 4).

Torsion experiments performed using the coarse-grained olivine tend to be well-reproducible at velocities higher than 0.1 m s^{-1}. This is due to the fast onset of mechanical weakening together with the lower amount of damage occurring at the sealing rings (PTFE). At slower velocities, damage induces abundant gouge extrusion. This effect is enhanced by the use of coarse-grained material (especially in the case of hard, granular silicates). Extrusion decreases the mechanical reproducibility and increases the number of failed runs. At these slow velocities (0.01 m s^{-1} and below), we could not provide reliable experiments using microgranular olivine nor retrieve samples for microstructural analyses.

Despite the lack of *in situ* temperature measurement, we can estimate a theoretical temperature, which is calculated as a function of slip velocity and hence friction coefficient, experiment duration and physical properties of the testing material (see section 2.2). The maximum temperature in nanoFo_{100} (sample 972) is 1491 °C for a velocity of 1 m s^{-1} and ~ 0.97 m of slip. In contrast, SC olivine sample 1007, deformed at similar slip velocity and to a similar final slip, reached only 1085 °C. The evolution of calculated temperature (Eq. 4) as a function of displacement and the evolution of the friction coefficient as a function of temperature for sample 1007 are both displayed in Figure 5. Sample 1007 is representative for all olivine samples deformed at 1 m s^{-1} (Fig. 3c and 4). Temperature increases steeply (~ 5.5 °C mm^{-1}) until stage III deformation is reached. During stage III, temperature continues to increase non-linearly (in the order of ~ 0.6 °C mm^{-1}) until dropping rapidly due to deceleration of the sample to arrest. The friction coefficient is negatively and non-linearly correlated to the calculated temperature during deformation. Upon deceleration, both the temperature and the friction coefficient increase until the deformation fully stops. We recall that olivine has a high melting temperature (for Fo_{90}, T_m = 1 765 °C at 0 GPa, and 2 075 °C at 6 GPa; Bowen and Shairer, 1935; Wang et al., 2016) and very slow Si lattice diffusivity (10^{-23} m^2 s^{-1} at 1200 °C; Fei et al., 2013). However, for the temperature estimates and durations of the experiments, the characteristic distances calculated from Si grain boundary and surface diffusivity (see materials and methods section) yield non-negligible values (up to $L_{diff} = 5.4\times10^3$ nm; $L^*_{diff} = 1.07\times10^3$ nm, see Table 1).

3.2 Microstructures (SEM and EBSD)

Images from SEM of samples deformed at 1 m s^{-1} and 0.01 m s^{-1} are displayed in Figures 6 and 7 for nanoFo_{100} samples and in Figures 8 and 9 for SC and SB olivine.

As shown by comparison with Figure 2, imaging nanoFo_{100} samples by SEM was challenging due to strong electrostatic charging. Grain sizes in undeformed nanoFo_{100} powder vary between 50 and 100 nm and remain the same after deformation as shown by Figure 7. Note that sintering of the nano powder is only observed at the mirror surface (Fig. 7), not below. Even for samples deformed well within stage III (sample 972, see Fig. 3e), forsterite grains do not display significant growth or notable change in shape. At slip rates of 1 m s^{-1}, aggregates (clumps or clusters) of poorly sintered nanograins are visible for small values of displacement (nanoFo_{100} 984 and 987) near the presumed principal shear zone (PSZ). These clusters were also visible in the starting material, but do neither appear in the sample far from the PSZ, nor in samples deformed to high slip (up to 1 m). Based on SEM images, the nanoFo_{100} samples deformed at slip velocities of 0.1 m s^{-1} and 0.01 m s^{-1} are similar to the ones deformed at 1 m s^{-1}, though lacking evidence of clusters.

The SC and SB olivine show microstructural zoning with grains remaining at the size of the starting material at the center, while a thin top layer with significantly reduced grain sizes (as low as 3 ± 1 μm) develops as illustrated in Figure 8 (see also Fig. S2). This fine-grained layer is parallel to the shear direction and shows an outermost (top) smooth mirror surface. Indeed, previous inspection by optical microscopy of the mirror-surfaces of our samples reveals frequent radial Riedel shear-like features at low angles to the shear plane (Fig. S2). Pluck outs are generally more abundant outside of the fine-grained layer than at the center (Figs. 8 and S4, and Table 2). While the border of the fine-grained zone towards the top is sharp, the grain sizes increase toward the center of the sample (i.e., bottom of the images in Figs. 8 and S4). For most of the samples, it is unclear if the fine-grained top layer of olivine represents the immediate vicinity of the PSZ (e.g., Smith et. al. 2011) or if the PSZ is partially lost during the difficult sample removal from the PTFE holder. Only sample 1095 displays a completely recovered and well preserved PSZ (Table 2). The recovered thickness of the fine-grained layer is reduced from 24 μm after 0.07 m of slip (sample 1012) down to 8 μm after ~1 m of slip (sample 1007). This apparent reduction in thickness could be related to a reduction of the PSZ thickness with increasing slip and/or to sample extraction.

A high magnification image of typical grain size and grain size distribution in SC olivine (sample 1012) near the PSZ, but not within the PSZ, is given in Figure 9. Grain with sizes up to 40 μm in diameter are surrounded by a matrix of significantly reduced grain size (enlarged in Fig. 9b and 9c). Large grains are dominantly sub-spherical, but angular to sub-angular grains with straight edges are likewise present. Additionally, grains often display intragranular cracks, especially at or close to grain edges. This later feature was also observed in the cold-pressed starting material (Fig. 2e).

As mentioned in the materials and methods section, despite tenacious tries, the large interaction volume of the electron beam (at least several dozen nm depending on the acceleration voltage and the beam current) did not allow satisfying detection of Kikuchi patterns in nanoFo_{100} samples, and hence prohibited their EBSD analysis (Fig. S3). Only SC and SB olivine samples were successfully analyzed by EBSD and later by TEM.

The microstructural parameters obtained by EBSD maps acquired on SB and SC olivine for key sample sections (e.g., PSZ or borders) are compiled in Table 2. EBSD could identify neither an amorphous phase such as intergranular melt, nor any relevant phases except for olivine. The key microstructural parameters are compiled in Figure 10. All deformed SB and

SC samples show important grain/clast size reduction in the PSZ. Average grain sizes calculated as the grain equivalent diameter for each map range from 73 μm in the undeformed SC starting material (sample 1009) to as low as 1.5 μm in SC olivine deformed at high strain rates and to a high slip (e.g., sample 1095, 0.47 m s^{-1} 0.99 m). If we extract the average grain size from samples deformed at the same velocity only (1 m s^{-1}), the grain size reduction is striking and occurs rapidly (< 0.2 m of slip, Fig. 10a). The decrease is also occurring for the maximum grain size (Fig. 10b), while the minimal grain size is *de facto* limited by the step size of the EBSD maps (Table 2).

The mean kernel average misorientation (KAM) which can be seen as a proxy for the density of geometrically necessary dislocations (see materials and methods section and e.g., Nye 1953; Adams 1997; Arsenlis and Park 1999), and therefore dislocation activity, does not vary significantly. KAM ranges from 0.21° in the undeformed starting material to a slightly higher value of 0.84° for highly deformed SC olivine (1007, 1 m s^{-1}, 1 m) as reported in Table 2, but all values remain below 1° and have a high standard deviation > 1.74°. Cataclastic flow is known to increase grain roundness/convexity (Ashby and Verrall, 1977), which is given by the PARIS parameter. The PARIS values increase with the amount of final slip, from 4.03 (sample 1009, SC starting powder) to 28.17 (sample 1095, 0.47 m s^{-1}, 1 m), as illustrated in Figure 10c. Note that very different EBSD step sizes will influence the calculation of the diameter, PARIS and KAM parameters; therefore, only samples with identical or similar step sizes should be compared to each other (Table 2).

Pole figures for each EBSD map (see Table 2) are shown in Figure 11, except for 1095 (Fig. 12). All CPO are extremely weak with no clear pattern. Calculated for one mean orientation per grain, the J-indexes (area weighted) are always low and apparently decrease from 3.2 – 4.2 in the starting material (cold-pressed San Carlos 1009, i.e., typical for cold-pressed aggregates, see Thieme et al., 2018) down to very low values of 1.0 (Fig. 10d) for sample 1007. Also, as previsouly reported by Gasc et al. (2019), when the number of measured grains is very high (N > 10,000), a pattern emerges in the pole figures while the J-index is very low (Fig. 11, sample 1007).

Both sides of the PSZ of experiment 1095 were successfully recovered (i.e., no splitting at the mirror surface) and experiment 1095 was thus selected for further detailed EBSD investigation. The band contrast, orientation map, misorientation to the grain mean and pole figures of texture for sample 1095 are compiled in Figure 12. The PSZ is characterized by significantly reduced grain sizes and porosity (Table 2), divided by a mirror surface defining two sides with unequal thickness. The grains outside of the vicinity of the PSZ (in areas 1 and 4) appear to be less rounded and exhibit a stronger heterogeneity in grain size. Rarely, large grains (i.e., > 30 μm) are in direct contact with the mirror surface. The internal misorientation is generally low (< 2°), mostly concentrating on the grain borders, especially at contact points between large grains. Subgrain boundaries can rarely be observed in large grains (Fig. 12c). Large grains are angular with irregular grain boundaries as already shown in Fig. 9, while small grains (i.e., < 30 μm) show curved grain boundaries, and even triple-junctions at differing angles, typical for a transient texture far from equilibrium.

The crystal preferred orientations (CPO) reported in Fig. 12d show a very weak texture close to the PSZ (area A2 and A3) while other areas (A1 and A4) have no noticeable texture: in A2 and A3 the [010] axes are perpendicular to the shear plane and the [001] axis seems parallel to the shear plane. The development of plastically deformed texture of our samples can be quantified using the texture J-index, but here all values remain very low (1.2 to 1.3, Fig. 12d). Furthermore, the orientation of the grain long axis displays a significant shape preferred orientation (SPO) parallel to the shear plane after low amounts of slip (e.g., in sample 1007, mean aspect ratio = 1.45 ± 0.3) as illustrated in Figure 13. This SPO is likely influenced by the initial shape of crystallites in the starting olivine powder and by perfect cleavage of olivine on (010) (see Fig. 2c, mean aspect ratio, 1.8 ± 0.6).

3.3 Nanostructures (TEM)

We selected a sample section inside and perpendicular to the PSZ of sample 1095 for TEM investigation. TEM images and high-resolution (HR-) TEM images of grain boundaries are shown in Figure 14. Grains exhibit both curved and straight well-sealed (sintered) grain boundaries, rare pores at triple junctions and nanometric bubbles inside of the grains as shown in Fig. 14a. These bubbles are not associated with dislocations or subgrain boundaries (see white arrows in Fig. 14a). Similar nanoscale bubbles have already been previously identified in San Carlos olivine (Mosenfelder et al., 2011; Burnard et al., 2015; Delon et al. 2018). Grains with sizes of < 200 nm are frequently located in pores at triple junctions (black arrows in Fig. 14a). Dislocation activity is low, with only a few well developed subgrain boundaries. Dislocations are straight or only slightly curved, indicating low lattice friction (Fig. 14b lower right grey grain). Pores and grain boundaries do not appear to be preferential sources or sites of dislocation activity. High resolution TEM images of grain boundaries in Figure 14c and 14d display long section of completely sintered, fully crystalline material and no evidence of melt or other amorphous (weak) phases along boundaries or at triple junctions.

4 Discussion

As already presented in the introduction, several mechanisms have been proposed to explain the drastic decrease of the friction coefficient in minerals when sheared at seismic slip rates: (1) Frictional melting; (2) flash heating/weakening; (3) an *a priori* presence of weak mineral phases, acting as a lubricant; (4) thermal expansion/pressurization; (5) phase transformations, i.e. thermally induced decomposition, which could again act as a lubricant and (5) a specific type of (melt-free) viscous flow, not physically defined yet. Additionally, cataclasis is likely involved at an early stage of the torsion experiments. Nevertheless, a satisfying common consensus based on observables from various materials has not yet been reached. We discuss below the relevance of each hypothesis, after a comparison with the literature.

4.1 Comparison with previous data

The stage III friction coefficients from this study and previous experiments at seismic slip rates are compiled in Figure 15. Most of the existing data are limited to felsic, metamorphic or carbonate rocks (e.g., Weeks and Tullis, 1985; Di Toro et al. 2004; Di Toro et al. 2006b; Hirose and Bystricky, 2007; Mizoguchi et al. 2007; Nielsen et al. 2008; Del Gaudio et al. 2009, Demurtas et al., 2019). Nevertheless, the friction coefficients from our experiments agree with previous mechanical data obtained on peridotites, but also on other lithologies as shown in Figure 15. The frictional strength of our monomineralic olivine aggregates reaches values of up to 0.36 in late stage III (0.26 in average, see Table 2, Fig. 6), which is higher than values reported previously for peridotites by Del Gaudio et al., 2009 (0.13-0.19 for a velocity of 1.14 m s^{-1}), and by Di Toro, 2006b (0.17-0.23 for a velocity of 1.14 m s^{-1}), who used two solid cylinders of natural polymineralic peridotites with grain sizes of ~ 0.7 mm from Balmuccia (Italy; with a modal composition of 71 % olivine, 21 % clinopyroxene, 4 % orthopyroxene, 4 % spinel + opaque minerals). The differences in experimental set up (rock versus powder) and chemical composition of the material (25 % of pyroxenes versus pure olivine) explain well the slight difference in friction coefficients. Also note that here the onset of dynamic weakening already occurred after a slip of only about 0.1 m and at a velocity of 0.01 m s^{-1}, which matches observations that the drop of friction stress (i.e., seismic-stress reduction) is similar for small and large earthquakes (see Marone, 2004, where this holds true over at least six orders of magnitude in fault dimension).

4.2 Grain size reduction by cataclastic flow

The internal fractures (Fig. 9), formation of a significant SPO (Fig. 13), reduction of CPO (i.e. decrease of J-index, Fig. 10d) and increase in grain roundness (i.e. PARIS values, Fig.10c) suggest that the deformation mechanism active during stage I and stage II deformation of micron-sized samples exhibits brittle behavior, i.e. cataclastic flow (Sibson 1977, 1986; Blenkinsop 2000). Cataclastic flow generally takes place under upper crustal conditions within the elasto-frictional regime, accommodating deformation by frictional sliding and rotation of fragmented grains (Sibson, 1977; Tullis and Yund, 1987; Babaie et al., 1991; Cladouhos, 1999). Cataclasis involves progressive grain fragmentation through frictional abrasion and penetrative fracturing (e.g. Engelder, 1974; Hirth and Tullis, 1994; Rawling and Goodwin, 2003). Once clasts reach a material-dependent grain size, the energy required for fracturing becomes too large and a fine-grained matrix, which embeds larger clasts, is formed (e.g., Mitra, 1984; Means, 1990). This weaker matrix (Fig. 9) dampens stresses from neighboring larger clasts and therefore allows large displacements as well as formation of foliation by granular flow (e.g., Chester et al., 1985; Marone et al. 1990; Hayman et al., 2004). Furthermore, if Riedel shears occur, they are expected to aid flow where the maximum shortening direction is roughly perpendicular to the foliation of the cataclasite (defined by the SPO of the clasts; Chester and Logan 1987; Marone and Scholz, 1989; Mair et al., 2002; Collettini et al., 2009). Optical microscopy of the mirror-surfaces of our samples reveals frequent radial Riedel shears (Fig. S2) at a low angle to the foliation, indicating a shortening along the rotation axis. As expected, we observed the most important grain size reduction close to the highest strain rate zone – in the top layer of the sample, close to the rotating top piston (shown in Figure 1; data are reported in Table 2). Additionally, cataclastic flow should reduce CPO strength, (e.g., Hutter et al., 1994, see also a rare example of weak CPO in calcite and dolomite, Demurtas et al. 2019), which is indeed observed (Table 2, Fig. 10).

The comparison of SC and SB with the deformed nanoFo_{100} samples is imperative as the olivine starting grain size was 70 nm. Deformation did not induce grain size reduction in nanoFo_{100}, and no layering in grain size was observed using SEM (Fig. 6 and 7). Furthermore, nanoFo_{100} samples display the same friction coefficient weakening as coarse-grained SC and SB olivine (Figure 2 and 4). Thus, our set of experiments permits to exclude cataclastic reduction of grain size as the weakening mechanism. However, it can be a fundamental prerequisite for dynamic weakening in the partially sintered PSZ.

4.3 Grain size reduction by thermal expansion

Thermal expansion can provide an alternative driving force for grain size reduction, especially if fluids are present in pores (e.g., Viesca and Garagash, 2015). Thermal expansion in olivine is anisotropic, resulting in a linear increase with temperature of *b* and *c* lattice parameters and a second order parabolic increase of the *a* lattice parameter and cell volume (Singh and Simmons, 1976). Hence, in a fluid-free system, the instantaneous expansion coefficient of *b* and *c* are constant, while the instantaneous expansion coefficient of the *a* lattice parameter increases with temperature. The total pressure $P_{(\nu,T)}$ inside the sample can be divided into two components,

$$P_{(\nu,T)} = P_{(\nu,Ti)} + \Delta P_{(th)} \qquad \text{eq. (10)}$$

where $P_{(\nu,T)}$ is the isothermal equation of state and $\Delta P_{(th)}$ is the thermal pressure due to annealing of a material at constant volume from an initial temperature T_i to the final temperature T (Kroll et al., 2012). In our fluid-free experiments, heating forsterite from room temperature to at least 900 °C - a plausible temperature experienced by all samples deformed at 1 m s^{-1} reaching stage III deformation - results in a thermal pressure $\Delta P_{(th)}$ of approximately 3.4 GPa, assuming constant volume (Kroll et al., 2012). At this temperature, the lattice parameters of San Carlos olivine increase by 0.69 % for *a*, 1.07 % for *b* and 1.00 % for *c* (Singh and Simmons, 1976). The imposed low normal stress of 20 MPa during our experiments allows for relaxation of stresses induced by thermal expansion, yet local radial stresses in a sample with significant SPO (Fig. 13) might enhance grain size reduction and therefore might provide a mechanism for thermo-mechanical weakening even if fluids are not present. Here again, thermal expansion can only be a prerequisite for - or accommodating mechanism to - dynamic weakening in the partially sintered PSZ.

4.4 Frictionally-induced melt

The maximum homologous temperature $T_H = 0.79$ achieved in our study is significantly below the melting temperature (for Fo_{90}, T_m = 1 765 °C and for Fo_{100}, T_m = 1 896 °C, at 20 MPa, Bowen and Shairer, 1935; Wang et al., 2016). As expected, we did not find evidence of phase reaction, transition, decomposition or melt genesis in EBSD and EDS analyses, SEM images (e.g., no decrease in contrast at the rims of olivines, Fig. 9) and in HR-TEM images of grain boundaries of the deformed samples (Fig. 14c and d). Thus, thermal decomposition, melting and *a priori* presence of weak phases located at grain boundaries, phase transition or even thermo-chemical pressurization can be excluded as possible weakening mechanisms in olivine aggregates deformed at our experimental conditions. Flash heating/weakening, induced by load-bearing asperities, and would have generated temperature gradients above and below the PSZ (e.g., Rice 2006; Tullis, 2011), and thus a noticeable progressive sintering of the olivine matrix, which is not observed here (Fig. 12). The local high heat increase could also generate melt films at the PSZ. However, here we do not observe melt films with increasing thickness in the PSZ (HR-TEM images in Fig. 14), which are a necessity in the flash weakening model of Rempel and Weaver (2008). As in experiments from Pozzi et al., (2018, 2019), our microstructural observations do not support flash heating/weakening as the dominant mechanism in our experiments.

Occurrence of melt was previously reported by Del Gaudio et al. (2009) in Balmuccia peridotites (av. grain size of 0.7 mm) experimentally deformed in rotary shear at a velocity of

0.92 m s^{-1}, and under a normal stress of 13 MPa and no confining pressure. For their series of experiments, and to the contrary of the present study, we recall that the authors used two solid (polymineralic) natural peridotite cylinders, mimicking a single sliding interface where extreme localization of shear occurred very rapidly and generated large amounts of frictionally-induced melt. They report a range of calculated temperatures between 1100 °C and 1300 °C, achieved after ~ 20 m of slip. Despite the high melting temperature of diopside at 1350 °C, early partial melting in the form of precipitation of a silica enriched molten phase has been reported for temperatures as low as 1100 °C (Doukhan et al., 1993). This early partial melting phenomenon can explain rapid formation of melt observed by Del Gaudio et al. (2009), especially with the high clinopyroxene content of 21 % in the starting material. In our study, frictionally-induced melt would have been expected to occur if higher values of slip (> 15 m) were achieved. Here, we intentionally limited the finite slip in our experiments to identify if the dynamic weakening mechanism occurs before melting.

4.5 Stage III deformation mechanism

Results from deformation experiments in axial compression (without torsion) on fine grained olivine at lower strain rates (10^{-6} to 10^{-4} s^{-1}) and with a crustal confining pressure (300 MPa), but at comparable temperature ranges (800 - 1350 °C) report significantly higher stresses (> 50 MPa) for identical strain rates and grain sizes, as illustrated in Figure 16 (e.g. Hirth and Kohlstedt, 2003; Demouchy et al., 2013, 2014; Hansen et al., 2011; Ohuchi et al., 2015). Since pressure alone cannot explain the low stresses during stage III deformation, we expect variations in either microstructure or deformation mechanisms at the high slip rates and temperatures achieved during our experiments. The significant decrease of the friction coefficient above slip rates of 10^{-4} m s^{-1} in the literature data and for our samples (Figure 15) implies a deformation rate related weakening mechanism. Also, as suggested by Fig. 5b, the dominant deformation mechanism active during stage III deformation could be thermally activated. Additionally, since deformation during stage III is largely constrained within the PSZ, this stage is only reached after the mean grain size decreases below about 2 μm (Table 2).

Diffusion creep is a ductile (plastic) deformation mechanism that is both thermally activated and strongly enhanced in fine-grained rocks. Diffusion creep in olivine is controlled by Si lattice self-diffusion since Si is the slowest diffusing species (see Kohlstedt, 2007, for a review). Silicon self-diffusion coefficients in Fo_{90} and Fo_{100} (e.g. Fei et al., 2013; Dohmen et al., 2002) are very slow (10^{-23} m^2 s^{-1} at 1200 °C; Fei et al., 2013), even at the highest temperature reached in this study. Corresponding characteristic distances ($L^{Si}_{Lattice\ diffusion}$) are too short to explain the partially sintered microstructures observed in our deformed aggregates (Fig. 14, sample 1095). More proficient ionic diffusion mechanisms must occur, which here could be grain boundaries diffusion and surfaces diffusion. Using a proxy for Si grain boundary and surface diffusivity given by olivine grain growth equations from Karato (1989), it yields much faster diffusion coefficients and thus much longer characteristic distances up to 5.4×10^{3} nm (Table 1), which could be responsible for the observed partial sintering. Indeed, the ionic self-diffusivity in crystalline solids depend mostly on vacancy concentration [V] as: $D_i \propto D_{vacancy} \times [V]$ (e.g., Nakamura and Schmalzried, 1983). Here, the addition of numerous grain boundaries (Fig. 14b), which are vacancy-enriched fast pathways when compared to the olivine lattice ($D^{Si}_{grain\ boundary} > D^{Si}_{lattice}$) and free-surfaces linked to residual porosity must lead to a significant enhancement of the effective (bulk) diffusion coefficient during viscous deformation. An approximative formulation could be (following Chakraborty, 2008, his figure 8):

$$D^{Si}_{effective} \propto (D^{Si}_{lattice} + \frac{3\delta}{d} D^{Si}_{grain\ boundary} + \beta D^{Si}_{surface}) \qquad \text{eq. (11)}$$

where d is the grain size, δ the grain boundary thickness (consider be closed to 0.75-1 nm, see Hiraga and Kohlstedt, 2007, Burnard et al., 2015), and β is a coefficient related to free surface (and thus porosity). Note that even if the deformation experiments were not performed under typical upper mantle pressures, the locally high temperatures reached along and in PSZ in our experiments (e.g., 1085 °C, Fig. 5), whilst performed at room temperatures and therefore not strictly equivalent to hot mantle background temperatures, compare well to lithospheric temperatures and may support the applicability of our results to lithospheric-scale processes. A complex effective ionic diffusion including surface and grain boundaries should therefore act as a rapid accommodating and thus weakening mechanism of deformation at the PSZ, noticeable even over the short timescales of our experiments.

Mechanical weakening was previously reported in melt-free olivine as a function of increasing iron content but at slower strain rates (e.g., axial compression experiments by Zhao et al., 2009; Vickers indentation tests by Koizumi et al., 2020). Nonetheless, in our study the small difference in iron content (10 %) does not trigger a notable modification of the friction coefficient after the fine-grained microstructure was reached and for the quasi steady-state portion of the mechanical curves (Fig. 4). This lack of notable modification is probably due to grain boundary diffusion and surface diffusion easily overcoming the difference of Si lattice diffusion between iron-bearing (Fo_{91}) and iron-free olivine (Fo_{100}) (e.g., by the limited increase in vacancy concentration in Fo_{91} relative to Fo_{100}).

We conclude that frictional heating, effective ionic diffusion (combination of surface and grain boundary diffusion) and specific microstructures (i.e. fine-grain size and partial sintering) are the main prerequisites for friction coefficient reduction in melt-free olivine below Byerlee's values (cf. Byerlee, 1978). Furthermore, the frequency of remaining pores and curved grain boundaries demonstrate a transient texture and an ongoing sintering process at high temperatures relevant for the lithosphere. Since the normal stress is low (20 MPa), grain boundary activity (e.g., grain boundary sliding and migration) might accommodate significant amounts of strain without the need for another strong accommodating mechanism. However, in this study, we do not observe pervasive geometric void/cavity formation (Figs. 8, 9, 12a), which is typical of grain boundary sliding (e.g., Gasc et al., 2019).

Ionic diffusion as an accommodating mechanism is possible, but remains limited by the short duration of our experiments. Nevertheless, even if there is an overall low dislocation and grain boundary activity, it is likely that more than one ductile deformation mechanism is active during stage III deformation. Thus, reduction of friction coefficients below Byerlee's values (cf. Byerlee, 1978) could be explained by a combination of thermally activated grain boundary sensitive mechanisms and ongoing grain size insensitive deformation mechanisms.

5 Conclusions

Nano- (0.07 µm) to micro (70 µm) olivine aggregates have been deformed at seismic slip rates up to 1 m s^{-1} in rotary shear. Both mechanical data as well as microstructure have been characterized as a function of grain size, slip rate, chemistry and slip. Our main results are the following:

- For a slip rate of 1 m s^{-1}, friction coefficients drop from 0.8 down to < 0.4, independent of initial grain size. Quasi-steady state values are not significantly impacted by the iron content variation of the selected olivines (Fo_{90} vs Fo_{100}).

- Displacements as low as 0.1 m are sufficient to cause a reduction of the friction coefficient to ~ 0.3 for olivine, without genesis of melt.

- From SEM/TEM, cataclastic flow seems responsible for both the rapid early grain size reduction and increased grain roundness at the foremost stage of the torsion experiments, but not the decrease in friction coefficient.

- From EBSD, dislocation activity is very limited and dislocation creep cannot explain the achieved high strain rates.

- Deformation at seismic slip rates activates a melt-free, but temperature-sensitive deformation mechanism in olivine, leading to viscous behavior.

To conclude, even if diffusion creep appears active in the PSZ, it is likely that more than one ductile deformation mechanism is active during stage III deformation. Thus, the reduction of friction coefficients below Byerlee's values (cf. Byerlee, 1978) could be explained by a combination of thermally activated grain boundary sensitive mechanisms and ongoing grain size insensitive deformation mechanisms.

Acknowledgments

This project received funding from the European Union's Horizon 2020 research and innovation program under the Marie Sklodowska-Curie Grant agreement No. 642029. This study was partially supported by the JSPS KAKENHI grant (number JP18K03799) to S. K. and cooperative research program of the Earthquake Research Institute, Tokyo (Japan). We thank P. Cordier, A. Mussi and ODpin software for express help in indexing diffraction patterns, C. Nevado and D. Delmas for providing high-quality thin sections for SEM and TEM. We thank Dr. B. Mendis from the Department of Physics, Durham University for acquiring the TEM images. We are very grateful to G. Di Toro for providing a dataset helping to shape Figure 15, and to C. Thoraval and D. Mainprice for constructive discussion. We thank the editor and two reviewers for their constructive comments.

Data Availability

All raw mechanical and microstructural data are available upon request to the corresponding author.

References

Adams, B.L., 1997. Orientation imaging microscopy: Emerging and future applications. Ultramicroscopy 67 (1-4), 11–17. https://doi.org/10.1016/s0304-3991(96)00103-9

Andersen, T.B., and Austrheim, H., 2006. Fossil earthquakes recorded by pseudotachylytes in mantle peridotite from the Alpine subduction complex of Corsica, Earth Planet. Sc. Lett. 242, 58–72. https://doi.org/10.1016/j.epsl.2005.11.058

Andersen, T.B., Mair, K., Austrheim, H., Podladchikov, Y.Y. and Vrijmoed, J.C., 2008. Stress release in exhumed intermediate and deep earthquakes determined from ultramafic pseudotachylyte, Geology 36, 995–998, https://doi.org/10.1130/G25230A.1.

Arsenlis, A, Parks, D.M, 1999. Crystallographic aspects of geometrically-necessary and statistically-stored dislocation density. Acta Mat. 47 (5), 1597–1611. https://doi.org/10.1016/s1359-6454(99)00020-8

Ashby, M.F., and Verrall, R.A., 1977. Micromechanisms of flow and fracture, and their relevance to the rheology of the upper mantle, Phil. Trans. R Soc. Lond. Series A, Mathematical and Physical Sciences, 288, 59-95

Babaie, H.A., Babaie, A., Hadizadeh, J., 1991. Initiation of cataclastic flow and development of cataclastic foliation in nonporous quartzites from a natural fault zone. Tectonophysics 200, 67-77.

Bachmann, F., Hielscher, R., Schaeben, H., 2010. Texture analysis with MTEX – Free and open source software toolbox. Solid State Phenom. 160, 63–68. http://dx.doi.org/10. 4028/www.scientific.net/SSP.160.63.

Beeler, N. M., Tullis, T. E., Blanpied, M., Weeks, J., 1996. Frictional behavior of large displacement experimental faults, J. Geophys. Res. 101(B4), 8697 – 8715, doi:10.1029/96JB00411.

Blenkinsop, T., 2000. Deformation Microstructures and Mechanisms. Springer. p. 150.

Bolognesi, F., and Bistacchi, A., 2018. A km-scale “triaxial experiment” reveals the extreme mechanical weakness and anisotropy of mica-schists (Grandes Rousses Massif, France). J. Struct. Geol. 107, 53–63. https://doi.org/10.1016/J.JSG.2017.12.001

Bouchon, M., and P. Ihmlé, 1999. Stress drop and frictional heating during the 1994 deep Bolivia earthquake, Geophys. Res. Lett., 26(23), 3521–3524, doi:10.1029/1999GL005410

Bowen, N.L. and Schairer, J.F., 1935. Preliminary report on equilibrium-relations between feldspathoids, alkali-feldspars, and silica. Transactions, American Geophysical Union 16: doi: 10.1029/TR016i001p00325.

Braeck, S., and Podladchikov, Y.Y., 2007. Spontaneous thermal runaway as an ultimate failure mechanism of materials, Phys. Rev. Lett. 98, 095504–095508, doi:10.1103/PhysRevLett.98.095504.

Brantut N., Viesca, R.C., 2017. The fracture energy of ruptures driven by flash heating, Geophys. Res. Lett., 44, 6718–6725, https://doi.org/10.1002/2017GL074110.

Bridgman, P.W., 1936. Shearing phenomena at high pressure of possible importance for geology, J. Geol. 44, 653– 669.

Buening, D.K., Buseck, P.R., 1973. Fe-Mg lattice diffusion in olivine. J. Geophys. Res. 78, 6852–6862. http://dx.doi.org/10.1029/JB078i029p06852.

Bunge, H.-J., 1982. In: Texture Analysis in Materials Science. Butterworths, London, pp. 593

Burnard, P.G., Demouchy, S., Delon, R., Arnaud, N.O., Marrocchi, Y., Cordier, P., Addad, A., 2015. The role of grain boundaries in the storage and transport of noble gases in the mantle. Earth Planet. Sci. Lett. 430, 260–270. doi:10.1016/j.epsl.2015.08.024

Byerlee, J. D., 1978. Friction of rocks. Pure Appl. Geophys. 116, 615–626.

Carpenter, B. M., Marone, C., Saffer, D. M., 2011. Weakness of the San Andreas Fault revealed by samples from the active fault zone. Nat. Geosci. 4(4), 251–254. https://doi.org/10.1038/ngeo1089

Chakraborty, S., 2008. Diffusion in solid silicates: A tool to track timescales of processes comes of age. Ann. Rev. Earth Planet. Sci. 36, 153–190.

Chester, F.M., Friedman, M., Logan, J.M., 1985. Foliated cataclasites. Tecotnophysics, 111(1-2), 139-146.

Chester, F.M., Logan J.M., 1987. Composite planar fabric of gouge from the punchbowl fault, California. J. Struct. Geol. 9(5-6), 621-634.

Cladouhos, T.T, 1999 Shape preferred orientations of survivor grains in fault gouge, 1999. Shape preferred orientations of survivor grains in fault gouge. J. Struct. Geol., 21, 419-436.

Collettini C., Niemeijer, A., Viti, C., Marone, C., 2009 Fault zone fabric and fault weakness. Nature, 462(7275), 907-U98.

Crameri, F., Schmeling, H., Golabek, G. J., Duretz, T., Orendt, R., Buiter, S. J., May, D. A., Kaus, B. J., Gerya, T. V. and Tackley, P. J., 2012. A comparison of numerical surface topography calculations in geodynamic modelling: an evaluation of the 'sticky air' method. Geophys. J. Int. 189, 38-54. doi:10.1111/j.1365-246X.2012.05388.x

Crameri, F., and Tackley, P.J., 2015. Parameters controlling dynamically self-consistent plate tectonics and single-sided subduction in global models of mantle convection. J. Geophys. Res. Solid Earth 120, 3680–3706. https://doi.org/10.1002/2014JB011664.

De Paola, N., Hirose, T., Mitchell, T., Di Toro, G., Viti, C., Shimamoto, T., 2011. Fault lubrication and earthquake propagation in thermally unstable rocks. Geology 39(1), 35-38.

De Paola, N., Holdsworth, R. E., Viti, C., Collettini, C., Bullock, R., 2015. Can grain size sensitive flow lubricate faults during the initial stages of earthquake propagation? Earth Planet. Sci. Lett. 43, 48-58.

Del Gaudio, P., Di Toro, G., Han, R., Hirose, T., Nielsen, S., Shimamoto, T., Cavallo, A., 2009. Frictional melting of peridotite and seismic slip. J. Geophys. Res. Solid Earth 114(B6), B06306. https://doi.org/10.1029/2008JB005990

Delon, R., Demouchy, S., Marrocchi, Y., Bouhifd, M.A., Barou, F., Cordier, P., Addad, A., Burnard, P.G., 2018. Helium incorporation and diffusion in polycrystalline olivine. Chem. Geol. 488, 105–124. https://doi.org/10.1016/j.chemgeo.2018.04.013

Demouchy, S., 2010. Diffusion of hydrogen in olivine grain boundaries and implications for the survival of water-rich zones in the Earth's mantle. Earth Planet. Sci. Lett. 295, 305–313. http://dx.doi.org/10.1016/j.epsl.2010.04.019.

Demouchy, S., Mussi, A., Barou, F., Tommasi, A., Cordier, P., 2014. Viscoplasticity of polycrystalline olivine experimentally deformed at high pressure and 900°C. Tectonophysics 623, 123–135. http://dx.doi.org/10.1016/j.tecto.2014.03.022.

Demouchy, S., Tommasi, A., Ballaran, T.B., Cordier, P., 2013. Low strength of Earth's uppermost mantle inferred from tri-axial deformation experiments on dry olivine crystals. Phys. Earth Planet. Int. 220, 37–49. https://doi.org/10.1016/j.pepi.2013.04.008

Demouchy, S., Tommasi, A., Barou, F., Mainprice, D., Cordier, P., 2012. Deformation of olivine in torsion under hydrous conditions. Phys. Earth Planet. Int. 202-203, 57–70. https://doi.org/10.1029/2008GL036611

Demurtas, M., Smith, S.A.F., Prior, D.J., Spagnuolo, E., Di Toro, G., 2019. Development of crystallographic preferred orientation during cataclasis in low-temperature carbonate fault gouge. J. Struct. Geol.126, 37-50. https://doi.org/10.1016/j.jsg.2019.04.015.

Dietrich, J.H., 1979. Modeling of rock friction 1. Experimental results and constitutive equations. J. Geophys. Res. 84., 2161-2168.

Di Toro, G., Goldsby, D. L., Tullis, T. E, 2004. Friction falls towards zero in quartz rock as slip velocity approaches seismic rates. Nature 427, 436–439.

Di Toro, G., Hirose, T., Nielsen, S., Pennacchioni, G., Shimamoto, T, 2006a. Natural and experimental evidence of melt lubrication of faults during earthquakes. Science 311, 647–649.

Di Toro, G., Hirose, T., Nielsen, S., Shimamoto, T., 2006b. Relating High-Velocity Rock-Friction Experiments to Coseismic Slip in the Presence of Melts in Radiated Energy and the Physics of Faulting (eds. Abercrombie, R., McGarr, A., Di Toro, G. and Kanamori, H.) 121–134, Geophys. Monogr. Ser. 170, American Geophysical Union. Washington, D.C.

Di Toro, G., Han, R., Hirose, T., De Paola, N., Nielsen, S., Mizoguchi, K., Ferri, F., Cocco, M., Shimamoto, T., 2011. Fault lubrication during earthquakes. Nature 471(7339), 494–499. https://doi.org/10.1038/nature09838

Dohmen, R., Chakraborty, S., Becker, H.W., 2002. Si and O in olivine and implications for characterizing plastic flow in the mantle. J. Geophys. Res. 29, https://doi.org/1029–2002GL015480.

Doukhan N., Doukhan J.C., Ingrin J., Jaoul, O., Raterron, P., 1993 Early partial melting in pyroxenes. Am. Min. 78(11-12), 1246-1256.

Engelder, J.T., 1974. Cataclasis and generation of fault gouge. Geol. Soc. Am. Bull. 85 (10), 1515-1522.

Fei, Y., 1995. Thermal expansion. In Ahrens, T.J., (Ed.), Mineral physics and crystallography: A handbook of physical constants, American Geophysical Union, Washington, D.C. p. 29-44.

Fei, H., Koizumi, S., Sakamoto, N., Hashiguchi, M., Yurimoto, H., Marquardt, K., Miyajima, N., Katsura, T., 2018. Mg lattice diffusion in iron-free olivine and implications to conductivity anomaly in the oceanic asthenosphere. Earth Planet. Sci. Lett. 484, 204–212. https://doi.org/10.1016/j.epsl.2017.12.020

Fei, H., Wiedenbeck, M., Yamazaki, D., Katsura, T., 2013. Small effect of water on upper-mantle rheology based on silicon self-diffusion coefficients. Nature 213–215.

Ferri F., Di Toro G., Hirose T., Shimamoto T., 2010. Evidences of thermal pressurization in high velocity friction experiments on smectite-rich gouges. Terra Nova 22, 347-353

Frey, F.A., Prinz, M., 1978. Ultramafic inclusions from San Carlos, Arizona: petrologic and geochemical data bearing on their petrogenesis. Dev. Petrol. 5, 129–176. http://dx.doi.org/10.1016/B978-0-444-41658-2.50013-4.

Gasc, J., Demouchy, S., Barou, F., Koizumi, S., Cordier, P., 2019. Creep mechanisms in the lithospheric mantle inferred from deformation of iron-free forsterite aggregates at 900–1200 °C. Tectonophysics 761, 16–30. https://doi.org/10.1016/j.tecto.2019.04.009

Goldsby, D.L., and Tullis, T.E., 2002. Low frictional strength of quartz rocks at subseismic slip rates. Geophys. Res. Lett. 29, 1844.

Goldsby, D. L., and Tullis, T.E, 2011. Flash Heating Leads to Low Frictional Strength of Crustal Rocks at Earthquake Slip Rates. Science 334(6053), 216-218

Green, H.W., II, Shi, F., Bozhilov, K., Xia, G., Reches, Z., 2015. Phase transformation and nanometric flow cause extreme weakening during fault slip. Nature. Geosci. 8, 484–489. , https://doi.org/10.1038/ngeo2436

Griggs, D., and Handin, J., 1960. Observations on fracture and a hypothesis of earthquakes. Geol. Soc. Am. Mem. 79, 343– 373.

Han, R., Shimamoto, T., Hirose, T., Ree, J.-H., Ando, J, 2007. Ultralow friction of carbonate faults caused by thermal decomposition. Science 316, 878–881.

Han, R., Hirose, T., Shimamoto, T., 2010. Strong velocity weakening and powder lubrication of simulated carbonate faults at seismic slip rates. J. Geophys. Res. 115, B03412.

Hansen, L.N., Zimmerman, M.E., Kohlstedt, D.L., 2011. Grain boundary sliding in San Carlos olivine: Flow law parameters and crystallographic-preferred orientation. J. Geophys. Res. 116. https://doi.org/10.1029/2011JB008220

Hayman, N.W., Housen B.A., Cladouhos, T.T., Livi, K., 2004. Magnetic and clast fabrics as measurements of grain-scale processes within the Death Valley shallow crustal detachment faults. J. Geophys. Res. Solid Earth 109 (B5), B05409, , https://doi.org/10.1029/2003JB002902.

Hielscher, R., Schaeben, H., 2008. A novel pole figure inversion method: specification of the MTEX algorithm. J. Appl. Crystallogr. 41, 1024–1037. http://dx.doi.org/10.1107/S0021889808030112.

Hiraga, T., Kohlstedt, D.L., 2007. Equilibrium interface segregation in the diopside-forsterite system I: Analytical techniques, thermodynamics, and segregation characteristics. Geochim. Cosmochim. Acta 71, 1266–1280.

Hirose, T, and Bystricky M. 2007. Extreme dynamic weakening of faults during dehydration by coseismic shear heating. Geophys. Res. Lett. 34(14), L14311.

Hirose, T. and Shimamoto, T., 2005. Growth of molten zone as a mechanism of slip weakening of simulated faults in gabbro during frictional melting. J. Geophys. Res. 110, B05202.

Hirth, G., Kohlstedt, D.L., 2003. Rheology of the upper mantle and the mantle wedge: a view from the experimentalists, in: Eiler, J. (Ed.), Inside “The Subduction Factory”. American Geophysical Union, Washington D.C., p. 83–105.

Hirth, G., and Tullis, J. 1994. The brittle-plastic transition in experimentally deformed quartz aggregates. J. Geophys. Res. Solid Earth 99(B6), 11731-11747.

Hutter, K., Rajagopal, K.R., 1994. On flows of granular materials. Contin. Mech. Thermodyn. 6 (2), 81–139. https://doi .org /10 .1007 /BF01140894.

John, T., Medvedev, S., Rüpke, L.H., Andersen, T.B., Podladchikov, Y.Y., Austrheim, H., 2009. Generation of intermediate-depth earthquakes by self-localizing thermal runaway. Nat. Geosci. 2, 137 – 140, , https://doi.org/10.1038/ngeo419

Kanamori, H., Anderson, D. L., Heaton, T. H., 1998. Frictional melting during the rupture of the 1994 Bolivian earthquake. Science 279, 839–842, https://doi.org/10.1126/science.279.5352.839.

Karato, S.I., 1989. Grain growth kinetics in olivine aggregates. Tectonophysics 168, 255–273.

Kelemen, P. B., and G. Hirth, 2007. A periodic shear-heating mechanism for intermediate-depth earthquakes in the mantle. Nature 446, 787– 790, https://doi.org/10.1038/nature05717

Kohlstedt, D.L., 2007. Constitutive equations, rheological behavior, and viscosity of rocks, in: Schubert, G. (Ed.), Treatise in Geophysics, Elsevier. P 389-417.

Koizumi, S., Hiraga, T., Tachibana, C., Tasaka, M., Miyazaki, T., Kobayashi, T., Takamasa, A., Ohashi, N., Sano, S., 2010. Synthesis of highly dense and fine-grained aggregates of mantle composites by vacuum sintering of nano-sized mineral powders. Phys. Chem. Miner. 37(8), 505–518. https://doi.org/10.1007/s00269-009-0350-y

Koizumi, S., Hiraga, T., Suzuki, T.S., 2020. Vickers indentation tests on olivine: size effects. Phys .Chem. Miner. 1–14. , https://doi.org/10.1007/s00269-019-01075-5

Kroll, H., Kirfel., A., Heinemann, R., Barbier, B., 2012. Volume thermal expansion and related thermophysical parameters in the Mg,Fe olivine solid-solution series. Eur. J. Mineral. 24(6), 935-956.

Lynch, D.J., 1978. The San Bernardino volcanic field of southeastern Arizona. in: Land of Cochise (Southeastern Arizona), Callender, J. F.; Wilt, J.; Clemons, R. E.; James, H. L.; [eds.], New Mexico Geological Society 29th Annual Fall Field Conference Guidebook, 348 p.

Ma, S., Shimamoto, T., Yao, L., Togo, T., Kitajima, H., 2014. A rotary-shear low to high-velocity friction apparatus in Beijing to study rock friction at plate to seismic slip rates. Earthq. Sci. 27(5), 469–497. https://doi.org/10.1007/s11589-014-0097-5

Mackwell, S.J., Kohlstedt, D.L., Paterson, M.S., 1985. The role of water in the deformation of olivine single crystals. J. Geophys. Res. 90, 11319. , https://doi.org/10.1029/JB090iB13p11319.

Maerten, F., Madden, E.H., Pollard, D.D., Maerten, L., 2016a. Incorporating fault mechanics into inversions of aftershock data for the regional remote stress, with application to the

1992 Landers, California earthquake. Tectonophysics 674, 52–64. https://doi.org/10.1016/j.tecto.2016.01.032

Maerten, L., Maerten, F., Lejri, M., Gillespie, P., 2016b. Geomechanical paleostress inversion using fracture data. J. Struct. Geol. 89, 197–213. https://doi.org/10.1016/j.jsg.2016.06.007

Mair, K., Frye., K.M., Marone, C., 2002. Influence of grain characteristics on the friction of granular shear zones. J. Geophys. Res. Solid Earth, 107, B10, 2219. https://doi.org/10.1029/2001JB000516

Marone, C., 2004. Faults greased at high speed. Nature 427, 405-406.

Marone, C.J., Raleigh, C.B., Scholtz, C.H. 1990. Frictional behavior and constructive modeling of simulated fault gouge. J. Geophys. Res. Solid Earth 95, B5., 7007-7025. https://doi.org/10.1029/JB095iB05p07007

Marone, C.J., and Scholtz, C.H., 1989. Particle-size distribution and microstructure within simulated faults gouge. J. Struct. Geol. 11(7), 799-814.

Means, W.D. 1990. Kinematics, stress, deformation and material behavior. J. Struct. Geol. 12(8), 953-971.

Mei, S., and Kohlstedt, D., 2000. Influence of water on plastic deformation of olivine aggregates 1. Diffusion creep regime. J. Geophys. Res. 105, 21457–21469.

Mitra, G. 1984. Brittle to ductile transition due to large strains along the White Rock Thrust, Wind River Moutains, Wyoming. J. Struct. Geol., 6(1-2), 51-61.

Mizoguchi, K, Hirose, T., Shimamoto, T., Fukuama, E., 2007. Reconstruction of seismic faulting by high-velocity friction experiments: An example of the 1995 Kobe earthquake. Geophys. Res. Lett., 34(1), L01308.

Mizoguchi, K., Hirose, T., Shimamoto, T., Fukuyama, E., 2009. High-velocity frictional behavior and microstructure evolution of fault gouge obtained from Nojima fault, southwest Japan. Tectonophysics 471, 285–296.

Mosenfelder, J.L., LeVoyer, M., Rossman, G.R., Guan, Y., Bell, D.R., Asimow, P.D., Eiler, J.M., 2011. Analysis of hydrogen in olivine by SIMS: Evaluation of standards and protocole. Am. Min. 96, 1725–1741.

Nakagawa, T., and Tackley, P.J., 2015. Influence of plate tectonic mode on the coupled thermochemical evolution of Earth's mantle and core. Geochem. Geophys. Geosyst. 16, 3400–3413, https://doi.org/10.1002/2015GC005996.

Nakamura, A., and Schmalzried, H., 1983. On the nonstoichiometry and point defects of olivine. Phys. Chem. Miner. 10, 27–37.

Neville, S. L., Schiffman, P., Sadler, P., 1985. Ultramafic inclusions in late Miocene alkaline basalts from Fry and Ruby Mountains, San Bernardino Country, California. Am. Min. 70, 668-677.

Nielsen, S. and Di Toro, G, Hirose, T., Shimamoto, T., 2006. Constitutive law for melt lubrication on earthquakes faults. AGU Fall Meeting Abstracts.

Nielsen, S., Di Toro, G., Hirose, T., Shimamoto, T. 2008. Frictional melt and seismic slip. J. Geophys. Res. Solid Earth 113, B01308.

Nye, J.F., 1953. Some geometrical relations in dislocated crystals. Acta Metallurgica. 1 (2), 153–162. https://doi.org/10.1016/0001-6160(53)90054-6

Obata, M., and Karato, S., 1995. Ultramafic pseudotachylite from the Balmuccia peridotite, Ivrea Verbano Zone, northern Italy. Tectonophysics 242, 313– 328, https://doi.org/10.1016/0040-1951(94)00228-2.

Ogawa, M., 1987. Shear instability in a viscoelastic material as the cause of deep focus earthquakes. J. Geophys. Res. 92(B13), 13,801– 13,810, https://doi.org/10.1029/JB092iB13p13801

Ohuchi, T., Kawazoe, T., Higo, Y., Funakoshi, K.I., Suzuki, A., Kikegawa, T., Irifune, T., 2015. Dislocation-accommodated grain boundary sliding as the major deformation mechanism of olivine in the Earth's upper mantle. Sci. Adv. 1, e1500360–e1500360. https://doi.org/10.1126/sciadv.1500360

Piccardo, G.B., Coltorti, M., Grégoire, M., 2008. The Jurassic Ligurian Tethys, a fossil ultra-slow spreading ocean: the mantle perspective, Metasomatism in Oceanic and Continental Lithospheric Mantle. Geological Society, London, Special Publications 293: 11-33.

Pozzi, G., De Paola, N., Nielsen, S.B., Holdsworth, R.E., Bowen, L., 2018. A new interpretation for the nature and significance of mirror-like surfaces in experimental carbonate-hosted seismic faults. Geology 46(7), 583-586.

Pozzi, G., De Paola, N., Holdsworth, R.E., Bowen, L., Nielsen, S.B., Dempsey, E.D., 2019. Coseismic ultramylonites: An investigation of nanoscale viscous flow and fault weakening during seismic slip. Earth Planet. Sci. Lett. 516, 164–175. https://doi.org/10.1016/j.epsl.2019.03.042

Rawling, G.C., and Goodwin, L.B., 2003.Cataclasis and particulate flow in faults, poorly lithified sediments. J. Struct. Geol, 25(3), 317-331.

Reches, Z. and Lockner, D.A., 2010. Fault weakening and earthquake instability by powder lubrication. Nature 467, 452–455.

Rempel, A.W., and Weaver, S.L., A model for flash weakening by asperity melting during high-speed earthquake slip. J. Geophys. Res. 113, B11308 (2008).

Rice, J. R, 2006. Heating and weakening of faults during earthquake slip. J. Geophys. Res. 111, B05311.

Saffer, D. M., Bekins, B. A., Hickman, S., 2003. Topographically driven groundwater flow and the San Andreas heat flow paradox revisited. J. Geophys. Res. Solid Earth 108(B5), 405–406. https://doi.org/10.1029/2002JB001849

Scholz, C. H., 2000. Evidence for a strong San Andreas fault. Geology 28, 163–166

Scholz, C. H., 2002. The Mechanics of Earthquakes and Faulting. Cambridge Univ. Press.

Sibson, R.H., 1977. Fault rocks and fault mechanisms. J. Geol. Soc. 133 (3): 191–213. https://doi.org/10.1144/gsjgs.133.3.0191

Sibson, R.H., 1986. Brecciation processes in fault zones: Inferences from earthquake rupturing. Pure Appl. Geophys. 1241 (1–2): 159–175. https://doi.org/10.1007/BF00875724

Singh H.P., and Simmons, G., 1976. X-ray determination of thermal-expansion of olivines. Acta. Cryst. A, 32, 771-773

Smith, S.A.F., Billi, A. Di Toro, G., Spiess, R., 2011. Principal slip zones in limestone: microstructural characterization and implications for the seismic cycle (Tre Monti fault, central Apennines, Italy). Pure Appl. Geophys. 168, pp. 2365-2393.

Smith, S.A.F., Nielsen, S., Di Toro, G., 2015. Strain localization and the onset of dynamic weakening in calcite fault gouge. Earth Planet. Sci. Lett. 413, 25–36

Strating E.H.H., and Vissers R.L.M., 1994. Structures in natural serpentinite gouges. J. Struc. Geol. 16 (9), 1205-1215.

Sun, C., Liu, Y, Song, W., Fan, D., Wang, Z., and Tang, H., 2018. Thermodynamic properties of San Carlos olivine at high temperature and high pressure. Acta. Geochim. 37(2), 171-179.

Swiatlowski, J.L., Moore D.E., Lockner, D.A., 2018. Composition and strength of ultramafic-rich gouge from the Bartlett springs faults, California compared to Safod gouges: implications for fault creep. Geol. Soc. Am. Abstract, Vol. 50 (6). https://doi.org/10.1130/abs/20181M-316115.

Thieme, M., Demouchy, S., Mainprice, D., Barou, F., Cordier, P., 2018. Stress evolution and associated microstructure during transient creep of olivine at 1000–1200 °C. Phys. Earth Planet. Int. 278, 34–46.

Tielke, J.A., Zimmerman, M.E., Kohlstedt, D.L., 2017. Hydrolytic weakening in olivine single crystals, J. Geophys. Res. https://doi.org/10.1002/2017JB014004.

Tullis, J., and Yund, R.A., 1987. Transition from cataclastic flow to dislocation creep in feldspar - Mechanisms and microstructures. Geology, 15(7), 606-609.

Viesca, R.C. and Garagash, D.I., 2015. Ubiquitous weakening of faults due to thermal pressurization. Nat. Geosci. 8, 875–879.

Wallis, D., Hansen, L.N., Ben Britton, T., Wilkinson, A.J., 2016. Geometrically necessary dislocation densities in olivine obtained using high-angular resolution electron backscatter diffraction, Ultramicroscopy 168,34-45. https://doi.org/10.1016/j.ultramic.2016.06.002

Wang, L., Blaha S., Pintér, Z., Farla, R., Kawazoe, T., Miyajima, N., K. Michibayashi, K., Katsura, T., 2016. Temperature dependence of [100](010) and [001](010) dislocation mobility in natural olivine. Earth Planet. Sci. Lett. 441, 81-90

Weeks, J.D., and Tullis T.E., 1985. Frictional sliding of dolomite – A variation in constitutive behavior. J. Geophys. Res. 90(NB9), 7821-7826.

Xu, Y., Shankland, T.J., Linhardt, S., Rubie, D.C., Langenhorst, F., Klasinski, K., 2004. Thermal diffusivity and conductivity of olivine, wadsleyite and ringwoodite to 20 GPa and 1373 K. Phys. Earth Planet. Int. 143-144, 321–336. https://doi.org/10.1016/j.pepi.2004.03.005

Zhang, J.S., and Bass, J.D. 2016. Sound Velocities of olivine at high pressure and temperatures and the composition of Earth’s upper mantle. Geophys. Res. Lett. 34(18), 9611-9618.

Zhao, Y.H., Zimmerman, M.E., Kohlstedt, D.L., 2009. Effect of iron content on the creep behavior of olivine: 1. Anhydrous conditions. Earth Planet. Sci. Lett. 287, 229–240

Figure Captions

Fig. 1. Experimental assembly: (a) sample set up for torsion experiments; (b) top and bottom piston with sample post torsion; (c) recovered chips of deformed samples; (d) mounting step before epoxy impregnation; (d) polishing strategy.

Fig. 2. SEM images of the starting material assembly: (a) and (b) loose powder of nanoforsterite; (c) cold-pressed powder of nanoforsterite; (d) loose powder of olivine; and (e) cold-pressed powder of olivine.

Fig. 3 Friction coefficient as a function of displacement: (a) San Bernardino olivine with an initial grain size of 70 ± 2 µm deformed at 1 m s^{-1}; (b) San Bernardino olivine with an initial grain size of 70 ± 2 µm deformed at 1 m s^{-1}; (c) San Carlos olivine with an initial grain size of 70 ± 2 µm deformed at 1 m s^{-1} ; (d) San Carlos olivine with an average grain size of 70 µm deformed at 0.47 m s^{-1}; (e) nanoFo100 with an average grain size of 0.07 µm deformed at 1 m s^{-1} ; (f) nanoFo100 with an average grain size of 0.07 µm deformed at 0.1 m s^{-1}; (g) nanoFo100 with an average grain size of 0.07 µm deformed at 0.01 m s^{-1}; Roman numbers in red within in (a) identify the stages of deformation, see main text for details. Experiments considered as outliners are displayed with a thin line, while experiments selected for discussion are displayed with a thick line.

Fig. 4 Steady state analysis: Evolution of friction coefficients for a range of displacement 0.4-0.8 (m) for all samples showing steady state and additionally for 1.0-1.4 (m) for sample 1003, and for the same velocity of 1 m s^{-1}. Standard deviation on the average friction coefficient is shown as vertical bar. Grey dash line is the average from all experiments, black dash line is the results from the experiments with the lowest standard deviation (990, 1007, and 1003).

Fig. 5 Temperature estimates: (a) Calculated temperature as a function of displacement and (b) friction coefficient as a function of temperature for San Carlos olivine 1007 deformed in torsion at 1 m s^{-1} to 1 m of slip. Triangles mark the end of the torsion experiment.

Fig. 6. SEM images: Forward scattered electron image of (a) deformed nanoforsterite both deformed at 1 m/s ; sample 984 (0.11 m of slip) and (b) 987 (0.21 m of slip), and which show aggregates/clumps of nano powder close to the remains of the principal shear zone.

Fig. 7. SEM images: Forward scattered electron image of deformed nanoforsterite sample 972 (1 m/s and 0.97 m of slip) for three different magnifications. (a) Top of the sample, close to the remains of the principal shear zone with the mirror surface visible in the bottom left; (b) Mirror surface on top with the un-sintered powder below it; (c) Far from the principal shear zone.

Fig. 8. SEM images: (a) and (b) Forward scattered electron images of the deformed San Bernardino olivine 989; (c) Forward scattered electron images of the deformed San Carlos olivine 1007 and (d) 1012. The three samples were deformed at the same velocity (1 m/s), but have different final slip (0.94 m of slip for 989, 0.97 m of slip for 1007 and 0.07 m of slip for 1012).

Fig. 9. SEM images: Forward scattered electron image from near the finest grained zone in San Carlos olivine 1012 (1 m/s and 0.07 m of slip) with increasing magnification. The horizontal lines in (b) and (c) are scanning artifacts linked to holes in the sample surface.

Fig. 10. Statistical data from EBSD maps on olivine. Compilation for the area close to the principal shear zone (A2 or A3, see main text for details) for olivine deformed at the same

velocity. (a) Average grain size; (b) Maximal grain size; (c) PARIS parameter, and (d) J-index one point per grain.

Fig. 11. Pole figures for olivine samples: Lack of well-defined crystallographic preferred orientation in olivine aggregates in a lower hemisphere equal-area projection (see Table 2 for details). N indicates the number of grains and j stand for J-index (see materials and methods section for details).

Fig. 12. Microstructure characterization of sample 1095: (a) Band contrast image; (b) Crystallographic misorientation to a reference point (i.e., map center, marked with a black star); (c) Misorientation to the mean of each respective grain (Mis2Mean, see main text for details); And (d) pole figures of texture for sample 1095, deformed at 0.47 m s^{-1} and a slip of 0.99 m for each area (A1 to A4) marked in (a). The pole figures of texture and J-index have been calculated using the mean orientation of each grain. Note that area A1 is located outside and at the top of the principal shear zone (PSZ), area A2 and A3 represent both sides of the PSZ, on each side of the mirror surface, and area A4 is located outside and at the bottom of the PSZ. The number of grains considered for each pole figure is given by n, the percentage of non-index pixel (a proxy for porosity) is given by PNI. Note in (c) the presence of a few abnormal grains and grain portions with high misorientation (<15), which do not impact the CPO results.

Fig. 13. Rose diagram: Orientation of the long axis of the olivine grains relative to the shear plane. The sample of San Carlos olivine (1007) was deformed at 1 m s^{-1} to 1 m of slip and is representative for all the deformed samples of this study.

Fig. 14. TEM images: Section inside and perpendicular to the principal shear zone (PSZ) of sample 1095. (a) 3D sketch showing the full focus ion beam section and its orientation towards the PSZ and shear direction. White boxes give the position of the subsequent images (b), (c) and (d). White arrows indicate nano-bubbles, black arrows indicate nano size grains at triple junctions. (b) Zoom into the center grain showing few dislocations. (c, d) High resolution TEM images showing melt-free grain boundaries. Note the absence of intragranular cracks, the remaining porosity, the well-sealed and melt-free boundaries, and thus the partial sintering of the PSZ. Intragranular nanobubbles are common in San Carlos olivines (see Mosenfelder et al., 2011; Burnard et al., 2015).

Fig. 15 Evolution of friction coefficient as a function of log slip rate. Red symbols represent olivine aggregates from this study. Data from Dietrich et al. (1978), Shimamoto and Logan (1981), Weeks and Tullis (1985), Di Toro et al. (2004), Di Toro et al. (2006b), Han et al. (2007), Hirose and Bystricky (2007), Mizoguchi et al. (2007), Nielsen et al. (2008), Del Gaudio et al. (2009), Han et al., (2010) and Demurtas et al., (2019).

Fig. 16. Strain rate – Stress space. Comparison between the results from this study (quasi-steady state values from olivine and nanoFo100) and experimentally established flow laws for low temperature dislocation creep (Demouchy et al., 2013), high temperature dislocation creep (Hirth and Kohlstedt, 2003), diffusion creep (Hirth and Kohlstedt, 2003 for two different grain sizes and high and low temperature), and finally grain boundary sliding (Hirth and Kohlstedt, 2003; Hansen et al., 2011 and Ohuchi et al., 2015; for 1300 °C and fine grain size).

Table 1 Experimental conditions, mechanical results and calculated diffusive characteristic distances (L_{diff}) for each torsion experiment (NB: L_{diff} includes the progressive increase in temperature with friction and time, while L^*_{diff} is calculated for a fixed maximal temperature for the total duration of the experiment, see main text for details).

Experimental conditions						**Mechanical results**															
Sample	Material	Grain size φ (μm)	Slip velocity V (ms^{-1})	Sampling freq. (kHz)	Target slip d_e (m)	Slip d_s (m)	Stress σ_s (MPa) Stage II	Early stage III	Late stage III	Friction coefficient μ Stage II	Early stage III	Late stage III	Shear strain γ Stage II	Early stage III	Late stage III	Shear strain rate $\dot{\gamma}$ (s^{-1}) Stage II	Early stage III	Late stage III	Temperature T_{max} (°C)	Diffusive characteristic distance Si L_{Diff} (nm)	L^*_{Diff} (nm)
	Nanoforsterite																				
1013	Nano Fo_{100}	~0.07	Cold-press step only																		
972	Nano Fo_{100}	~0.07	1	2	1.000	0.97	15.3	-	-	0.76	-	-	670	-	-	189	-	-	1491	5.4×10^{3}	1.07×10^{3}
973	Nano Fo_{100}	~0.07	1	2	0.030	0.04	14.6	-	-	0.73	-	-	648	-	-	129	-	-	290	3.2×10^{-3}	1.91×10^{-3}
981	Nano Fo_{100}	~0.07	1	2	0.085	0.08	15.8	-	-	0.79	-	-	586	-	-	119	-	-	555	6.3×10^{-1}	6.42×10^{-1}
982	Nano Fo_{100}	~0.07	1	2	0.085	0.08	15.7	-	-	0.78	-	-	1074	-	-	236	-	-	532	4.6×10^{-1}	4.61×10^{-1}
983	Nano Fo_{100}	~0.07	1	2	0.105	0.1	15.7	-	-	0.78	-	-	898	-	-	294	-	-	605	1.3	1.39
984	Nano Fo_{100}	~0.07	1	2	0.136	0.11	15.5	-	-	0.77	-	-	904	-	-	306	-	-	700	4.0	4.26
987	Nano Fo_{100}	~0.07	1	2	0.200	0.21	15.9	-	-	0.79	-	-	444	-	-	143	-	-	971	3.5×10^{1}	5.07×10^{1}
988	Nano Fo_{100}	~0.07	1	2	0.200	0.19	16.1	-	-	0.80	-	-	778	-	-	249	-	-	791	1.2×10^{1}	1.30×10^{1}
992	Nano Fo_{100}	~0.07	0.01	1	1.000	1	16.7	-	-	0.83	-	-	7460	-	-	154	-	-	305	1.1×10^{-1}	1.49×10^{-1}
993	Nano Fo_{100}	~0.07	0.01	0.5	3.000	2.87	15.6	-	10	0.78	-	0.50	12600	-	47800	155	-	165	389	1.8	2.09
994	Nano Fo_{100}	~0.07	0.01	0.5	2.600	2.67	17.2	12.8	11.4	0.86	0.63	0.56	10780	17960	44600	160	164	167	393	1.4	2.20
995	Nano Fo_{100}	~0.07	0.1	5	1.000	0.99	15.1	-	-	0.75	-	-	1348	-	-	1818	-	-	677	2.4×10^{1}	3.18×10^{1}
996	Nano Fo_{100}	~0.07	0.1	5	0.700	0.70	15.8	-	-	0.79	-	-	824	-	-	4071	-	-	703	1.7×10^{1}	3.50×10^{1}
997	Nano Fo_{100}	~0.07	0.1	5	2.000	1.99	15.4	-	-	0.77	-	-	2620	-	-	2541	-	-	737	5.9×10^{1}	8.23×10^{1}
998	Nano Fo_{100}	~0.07	0.1	5	2.000	1.88	15.6	-	-	0.78	-	-	2820	-	-	8309	-	-	759	8.7×10^{1}	9.80×10^{1}
999	Nano Fo_{100}	~0.07	0.1	5	0.160	0.16	15.4	-	-	0.77	-	-	2440	-	-	2540	-	-	362	5.1×10^{-2}	8.40×10^{-2}
1000	Nano Fo_{100}	~0.07	1	5	1.000	0.97	15	7.0	3.1	0.75	0.35	0.15	670	3060	16200	978	4256	18426	933	7.5×10^{1}	8.54×10^{1}
1003	Nano Fo_{100}	~0.07	1	5	1.500	1.46	15.8	7.3	5	0.79	0.36	0.25	668	2600	24400	287	1055	6463	1320	4.4×10^{2}	7.28×10^{2}
1005	Nano Fo_{100}	~0.07	1	5	1.500	1.45	15.8	7.3	3.9	0.79	0.36	0.20	692	2820	24000	223	869	5294	1264	4.5×10^{2}	5.82×10^{2}
1006	Nano Fo_{100}	~0.07	1	5	1.000	0.95	15.5	5.7	3.8	0.77	0.28	0.18	850	2980	19400	296	990	5124	938	6.6×10^{1}	8.74×10^{1}
	Olivine																				
1009	SC Olivine	70	Cold-press step only																		
989	SB Olivine	70	1	2	1.000	0.94	14.5	8.1	6.6	0.72	0.41	0.33	196	2200	15600	51	547	3227	1226	2.4×10^{2}	4.00×10^{2}
990	SB Olivine	70	1	2	1.000	0.93	15	7.8	5.1	0.75	0.39	0.25	244	2600	15600	69	697	3460	1078	4.0×10^{2}	1.97×10^{2}
1007	SC Olivine	70	1	5	1.000	0.97	14.4	6.8	5.1	0.72	0.34	0.25	306	2340	16200	117	844	4490	1085	1.3×10^{2}	2.09×10^{2}
1008	SC Olivine	70	1	5	0.170	0.12	15.8	-	-	0.79	-	-	256	-	-	99	-	-	600	1.5	1.43
1010	SC Olivine	70	1	5	0.600	0.58	16	7.4	5.7	0.80	0.37	0.28	248	2400	9800	91	823	2908	898	3.5×10^{1}	5.20×10^{1}
1011	SC Olivine	70	1	5	0.025	0.03	14.9	-	-	0.74	-	-	270	-	-	112	-	-	215	2.5×10^{-4}	1.20×10^{-4}
1012	SC Olivine	70	1	5	0.090	0.07	14.9	-	-	0.74	-	-	192	-	-	85	-	-	440	1.2×10^{-1}	9.22×10^{-2}
1095	SC Olivine	70	0.47	5	1.000	0.99	15.6	9.2	7.3	0.76	0.46	0.36	412	2440	16450	364	1737	5165	955	3.26×10^{2}	1.45×10^{2}

Table 2 Microstructural parameters obtained from EBSD maps of San Carlos and San Bernardino olivine samples. The samples are ranked as a function of increased final slip. We recall that the initial grain size for both batches of olivine powders was 70 ± 2 µm. All samples were deformed at 1 m s^{-1}, except for 1095, which was deformed at 0.47 m s^{-1}.

EBSD map	Area[a]	Slip (m)	Mapping step size (µm)	% Non - indexed[b]	Number of grains	Av. diameter[c] (µm)	and 1 σ	Max diameter (µm)	Min diameter (µm)	Av. PARIS[d]	and 1 σ	Av. KAM[e] (°)	and 1 σ	Texture J-index 1ppg[f]
1009_CI	Cold pressed olivine	0.00	2.0	76.7	66	66.58	1.65	164.68	22.34	4.27	4.90	0.21	1.99	3.2
1009_CII		0.00	2.0	78.8	42	72.91	1.43	129.79	35.00	4.03	4.15	0.21	2.15	4.8
1011_TI	A2	0.03	1.0	43.2	728	12.81	1.49	71.50	5.65	7.04	5.59	0.24	2.21	1.3
1011_CI	A0	0.03	0.5	50.2	1813	7.75	1.59	61.61	2.60	9.36	8.67	0.46	2.18	1.1
1012_TI	A1	0.07	2.0	44.8	271	2.87	1.35	5.22	1.45	6.34	5.24	0.75	1.74	1.7
1012_CI	A2	0.07	0.5	57.8	105	6.28	1.37	20.61	3.99	6.16	5.27	0.73	1.92	2.3
1008_TI	A1	0.12	2.0	22.8	271	6.08	1.48	20.23	3.18	8.44	7.97	0.76	2.02	1.6
1008_TII	A2	0.12	0.5	23.6	138	2.54	1.35	7.58	1.29	8.24	6.17	0.69	1.83	2.2
1008_CI	A0	0.12	0.5	41.4	7609	5.70	1.64	107.15	2.33	17.36	10.67	0.34	2.20	1.0
1008_CII	A0	0.12	0.5	48.7	2921	6.08	1.66	82.70	2.29	16.47	9.93	0.31	2.24	1.1
1010_TII	A2	0.58	0.5	17.9	618	4.46	1.51	40.75	2.34	21.17	12.20	0.57	1.90	1.3
990_TII	A2	0.93	0.3	19.2	344	2.69	1.42	14.35	1.40	23.41	11.21	0.80	1.74	1.8
990_CI	A0	0.93	1.0	29.6	635	13.03	1.67	68.68	5.38	14.12	8.94	0.48	1.86	1.4
990_CII	A0	0.93	1.0	30.7	1236	12.42	1.65	81.51	5.19	14.69	9.53	0.47	1.90	1.2
989_TI	A1	0.94	0.5	29.7	332	4.74	1.38	16.61	2.50	14.88	11.23	0.68	1.86	1.6
989_TII	A1	0.94	0.5	12.9	142	4.61	1.37	17.08	2.32	19.65	12.22	0.56	2.00	1.9
989_TIII	A2	0.94	0.3	32.7	150	2.79	1.47	7.06	1.48	20.41	12.72	0.75	1.82	2.1
1007_TI	A1	0.97	2.0	11.7	269	5.53	1.46	27.75	2.38	10.75	8.20	0.84	2.17	1.8
1007_CI	A0	0.97	0.2	30.0	11321	10.00	1.65	98.48	4.51	24.12	12.51	0.26	2.11	1.0
1095	A1+A2+A3+A4	0.99	0.2	18.2	4633	1.80	1.55	27.99	0.55	23.32	14.85	0.38	1.88	1.2
1095_I	A1	0.99	0.2	26.9	1199	1.96	1.62	21.60	0.55	15.36	11.78	0.41	2.02	1.2
1095_II	A2	0.99	0.2	7.4	2120	1.60	1.04	14.15	0.55	28.17	14.25	0.37	1.74	1.2
1095_III	A3	0.99	0.2	8.8	683	1.80	1.47	20.00	0.55	26.55	15.17	0.35	1.91	1.3
1095_IV	A4	0.99	0.2	18.9	747	2.04	2.32	27.99	0.55	16.22	12.01	0.38	1.87	1.3

a A0: far from the principal shear zone; A1 or A4: transition area; A2 and A3: area near the principal shear zone, above or below, see Figure 12 for illustration;
b: Proxy for porosity, see main text for details.
c: The grain size is calculated as the geometric mean of the log-normal distribution of the grain equivalent diameter (i.e., diameter of a sphere with equivalent area).
d: PARIS: Percentile average relative indented surface boundary, measure of the curvature of grain boundaries. A high PARIS indicates highly curved or indented boundaries.
e: KAM: Geometric mean of the log-normal distribution of the Kernel Average Misorientation (proxy for density of geometrically necessary dislocations), 2nd order, threshold of 5 °.
f: One point per grain (1ppg) uses the mean orientation of each grain for the calculation of the texture J-index (Bunge 1982, e.g., integral of the squared orientation distribution function).

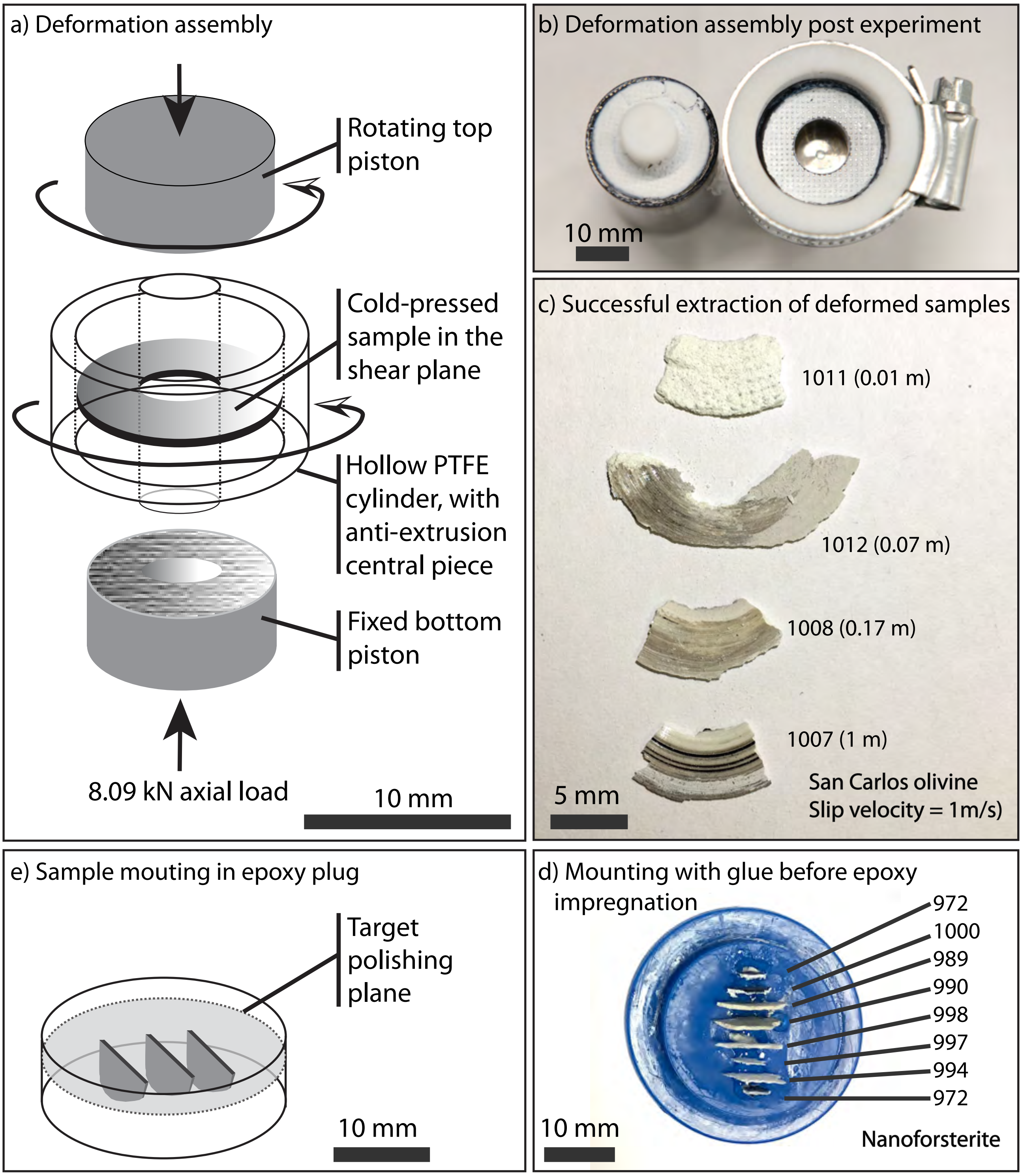

Fig. 1. Experimental assembly: (a) sample set up for torsion experiments; (b) top and bottom piston with sample post torsion; (c) recovered chips of deformed samples; (d) mounting step before epoxy impregnation; (d) polishing strategy.

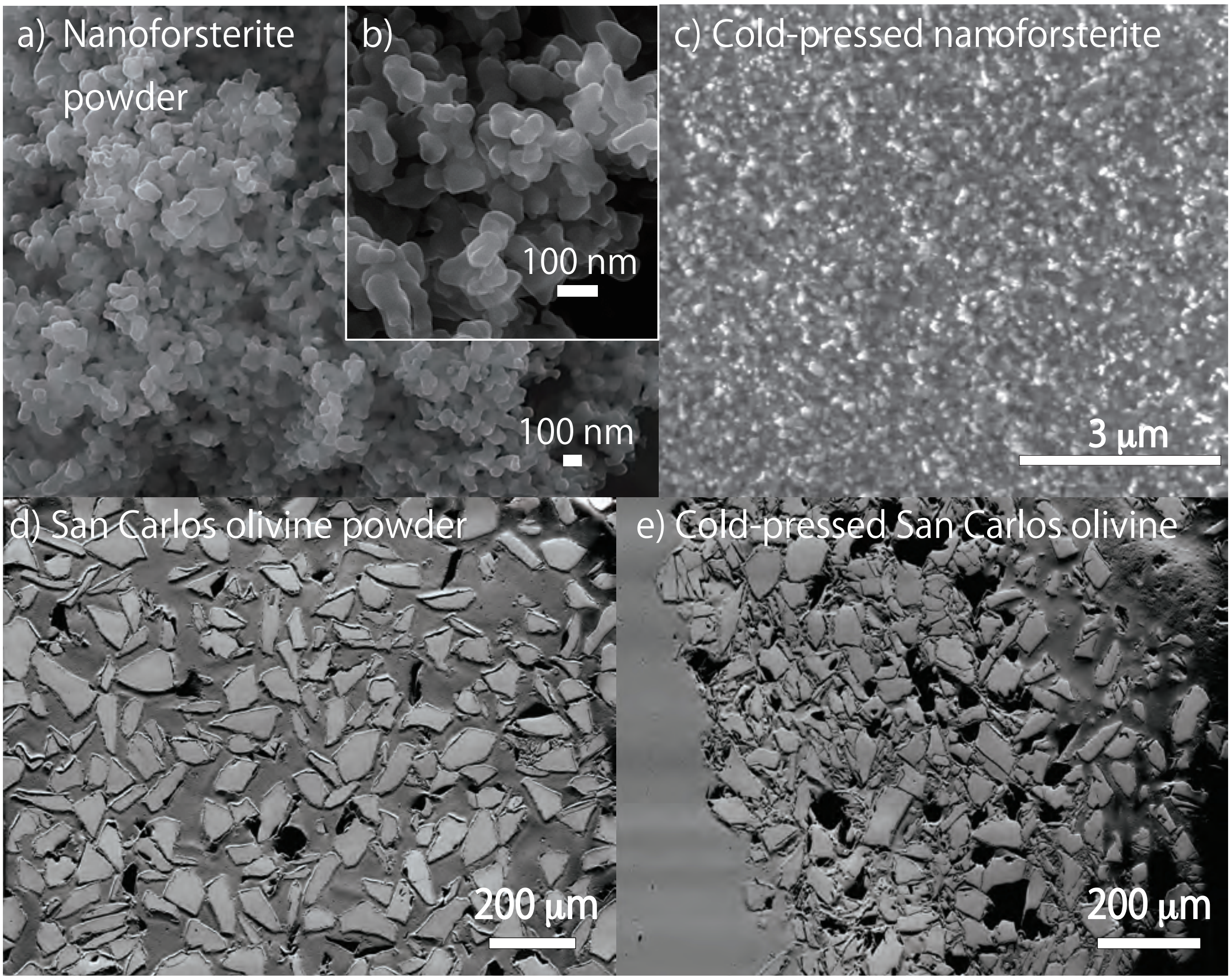

Fig. 2. SEM images of the starting material assembly: (a) and (b) loose powder of nanoforsterite ; (c) cold-pressed powder of nanoforsterite; (d) loose powder of olivine; and (e) cold-pressed powder of olivine.

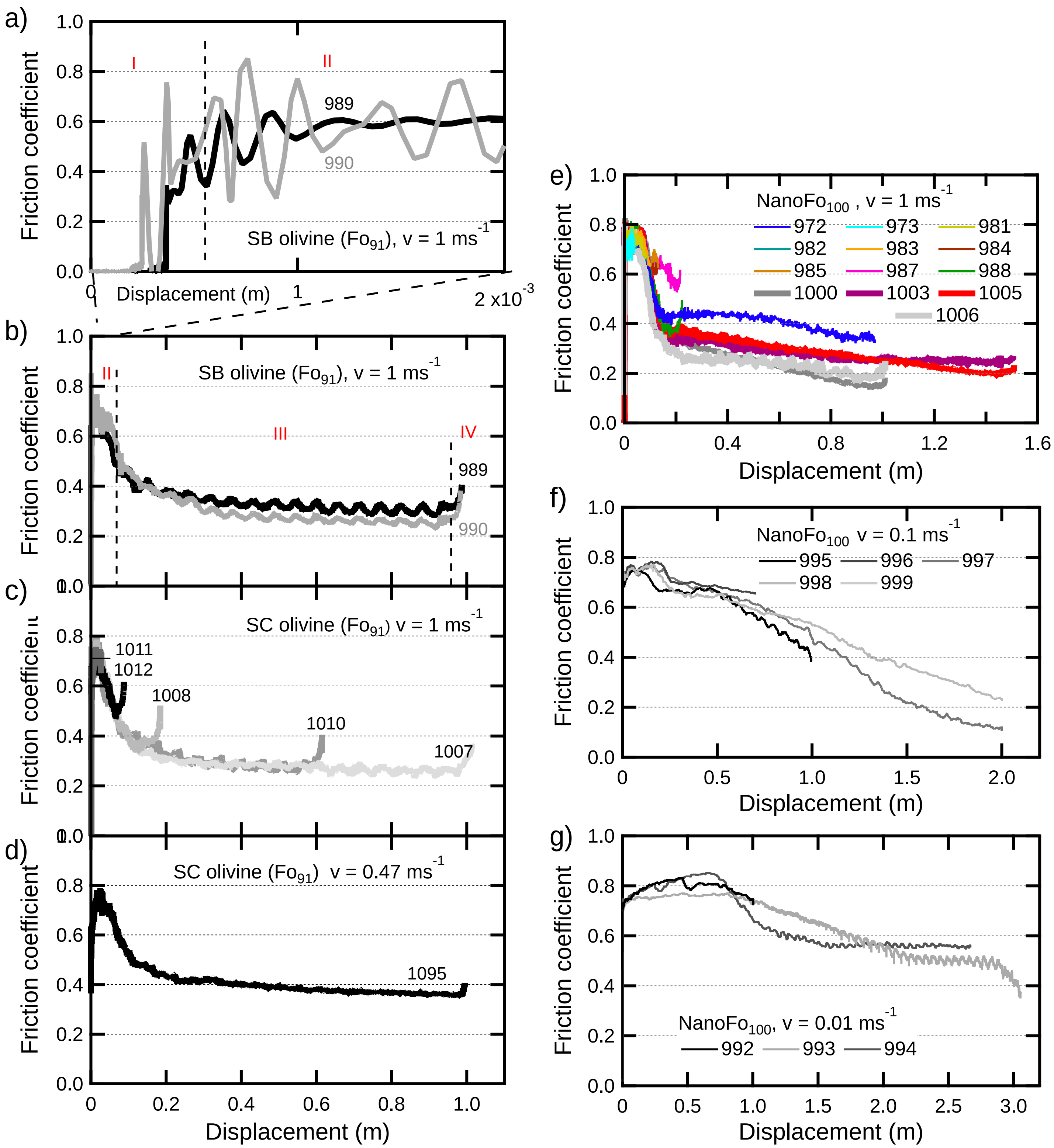

Fig. 3. Friction coefficient as a function of displacement: (a) San Bernardino olivine with an initial grain size of 70 ± 2 µm deformed at 1 ms^{-1}; (b) San Bernardino olivine with an initial grain size of 70 ± 2 µm deformed at 1 ms^{-1}; (c) San Carlos olivine with an initial grain size of 70 ± 2 µm deformed at 1 ms^{-1} ; (d) San Carlos olivine with an average grain size of 70 µm deformed at 0.47 ms^{-1}; (e) nanoFo100 with an average grain size of 0.07 µm deformed at 1 ms^{-1} ; (f) nanoFo100 with an average grain size of 0.07 µm deformed at 0.1 m^{-1}; (g) nanoFo100 with an average grain size of 0.07 µm deformed at 0.01 ms^{-1}; Roman numbers in red within in (a) identify the stages of deformation, see main text for details. Experiments concidered as outliners are displayed with a thin line, while experiments selected for discussion are displayed with a thick line.

Figure 4

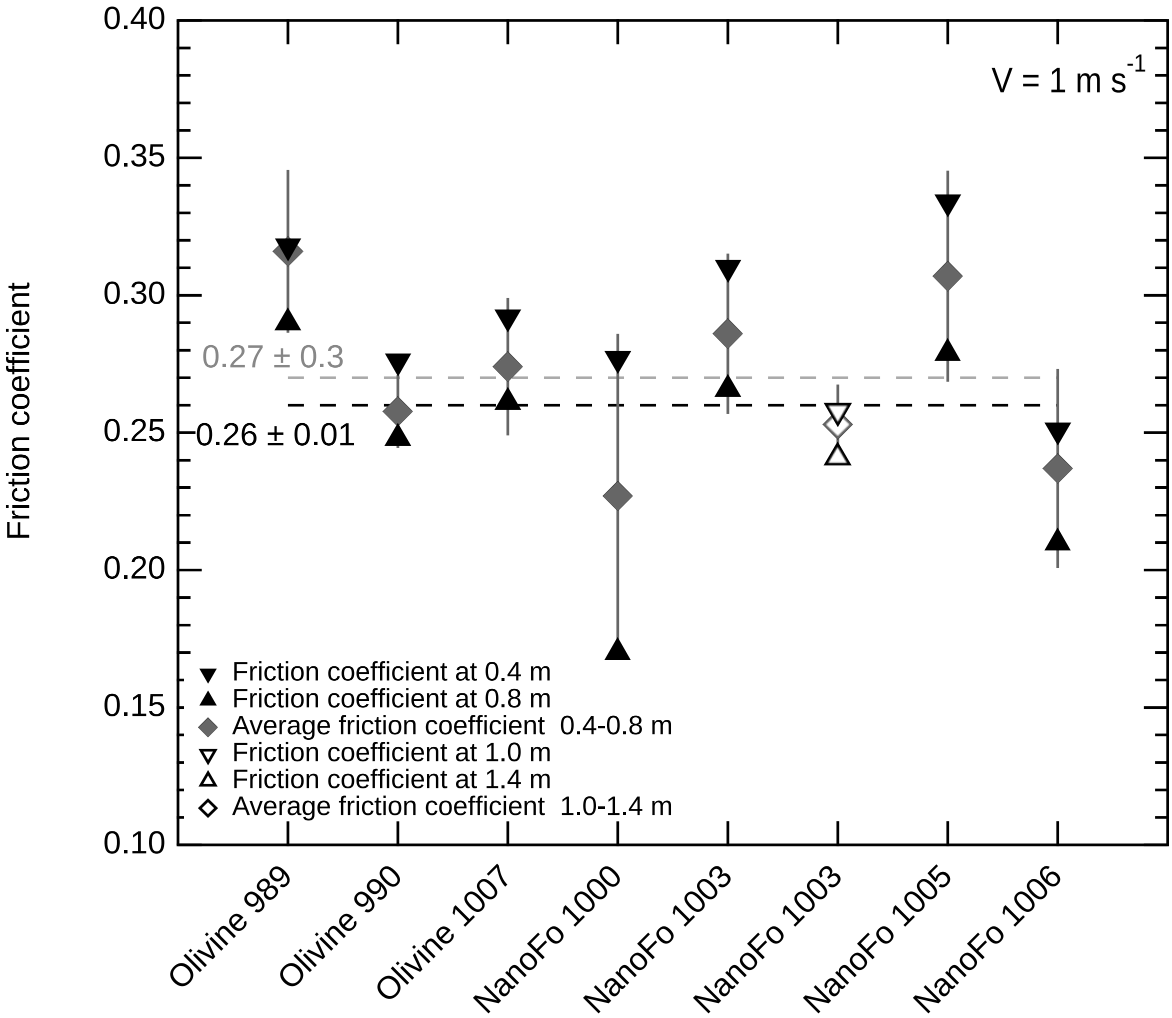

Fig. 4 Steady state analyse: Evolution of friction coefficients for a range of displacement 0.4-0.8 (m) for all samples showing steady state and additionally for 1.0-1.4 (m) for sample 1003, and at thre same velocity of 1 m s^{-1}. Standard deviation on the average friction coefficient is shown as vertical bar. Grey dash line is the average from all experiments, black dash line is the results from the experiment with the lowest standard deviation (990, 1007, and 1003).

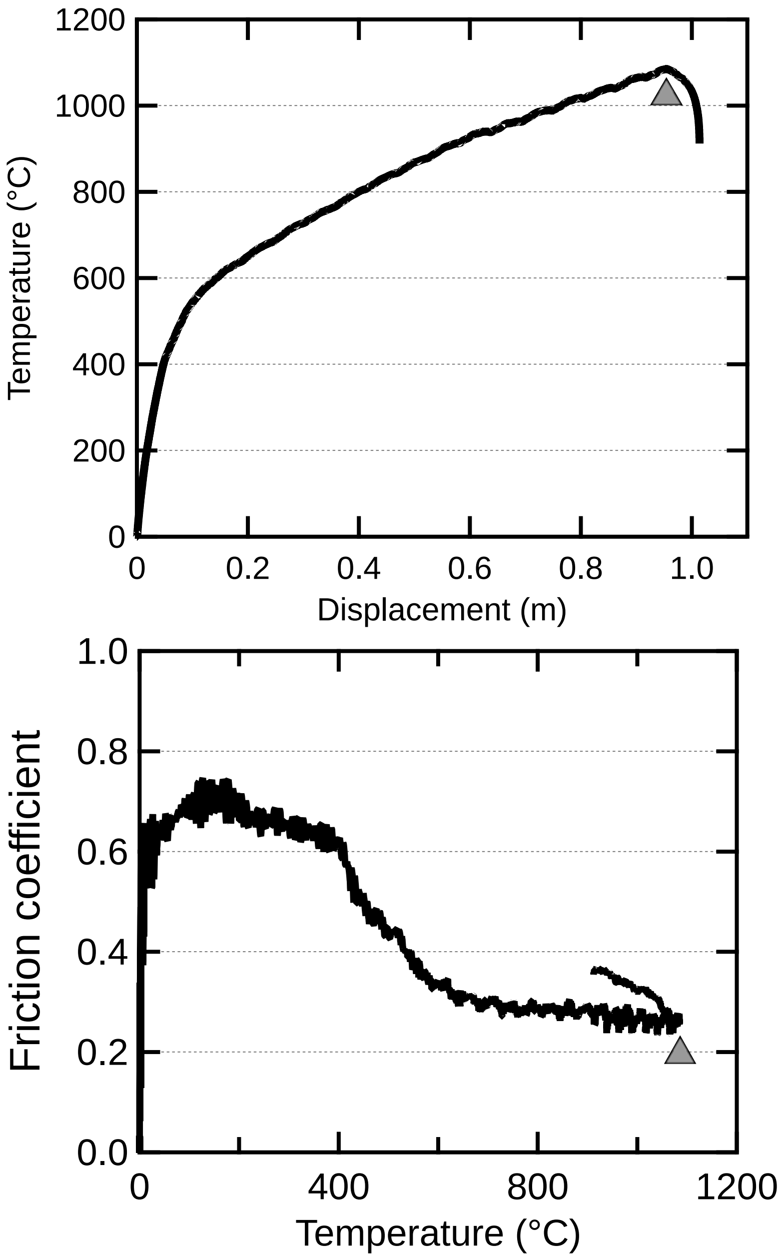

Fig. 5 Temperature estimates: (a) Calculated temperature as a function of displacement and (b) friction coefficient as a function of temperature for San Carlos olivine 1007 deformed in torsion at 1 ms^{-1} to 1 m of slip. Triangles mark the end of the torsion experiment.

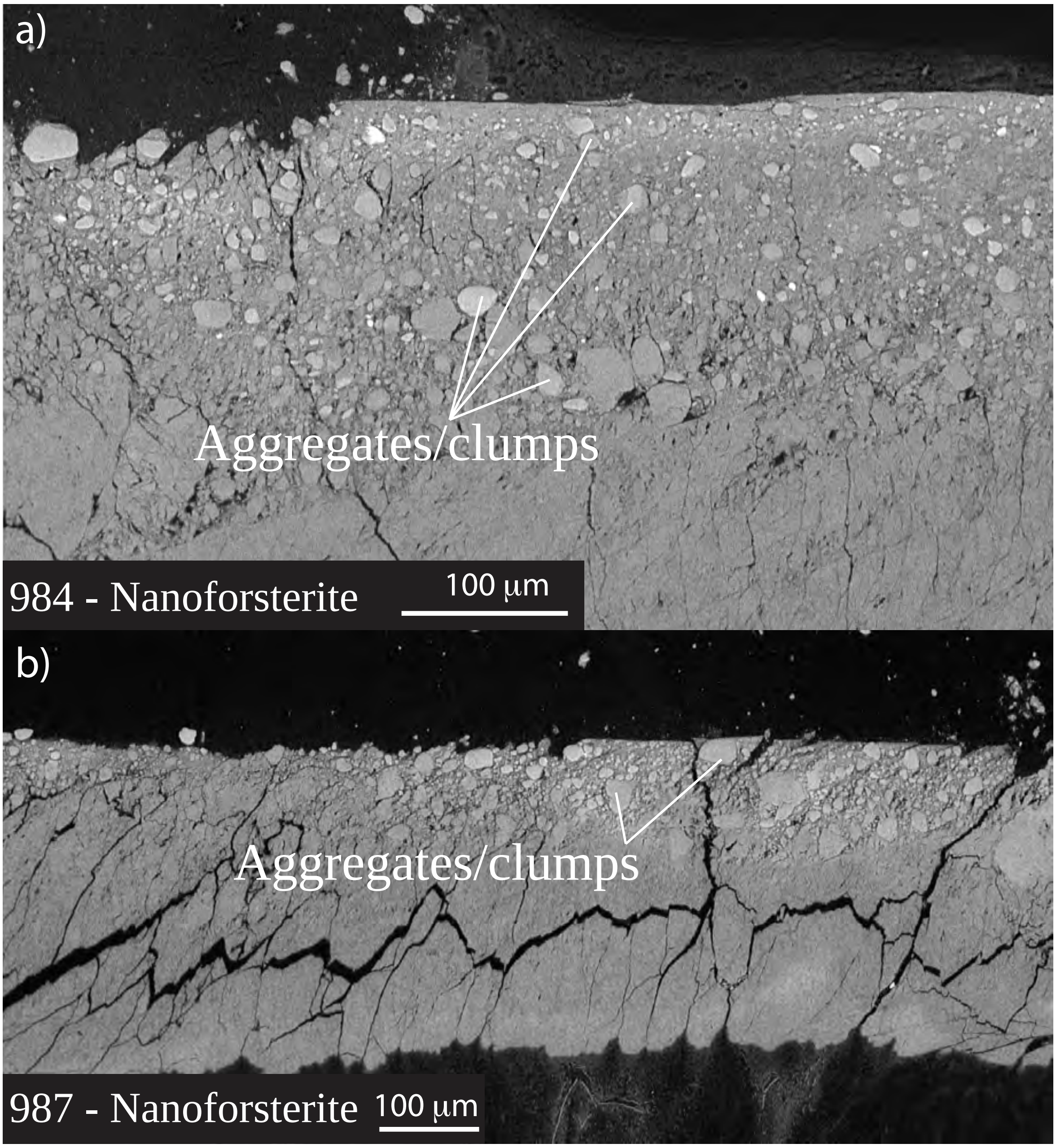

Fig. 6. SEM images: Forward scattered electron image of (a) nanoforsterite both deformed at 1 m/s ; sample 984 (0.11 m of slip) and (b) 987 (0.21 m of slip), and which show the aggregates/clumps of nanopowder close the remains of the principal shear zone.

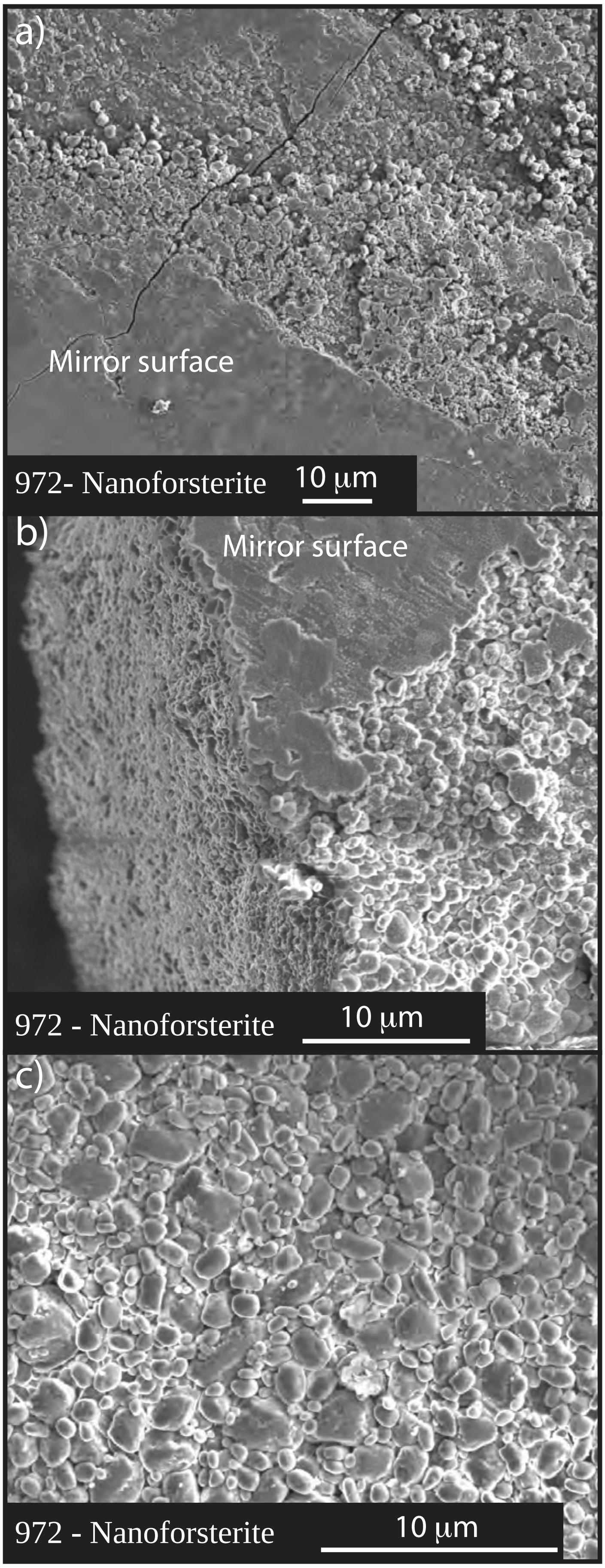

Fig. 7. SEM images: Forward scattered electron image of deformed nanoforsterite sample 972 (1m/s and 0.97 m of slip) for three different magnifications. (a) top of the sample, close to the remains of the prin cipal shear zone with the mirror surface visible in the bottom left; (b) mirror surface on top with the un-sintered powder below it; (c) far from the principal shear zone.

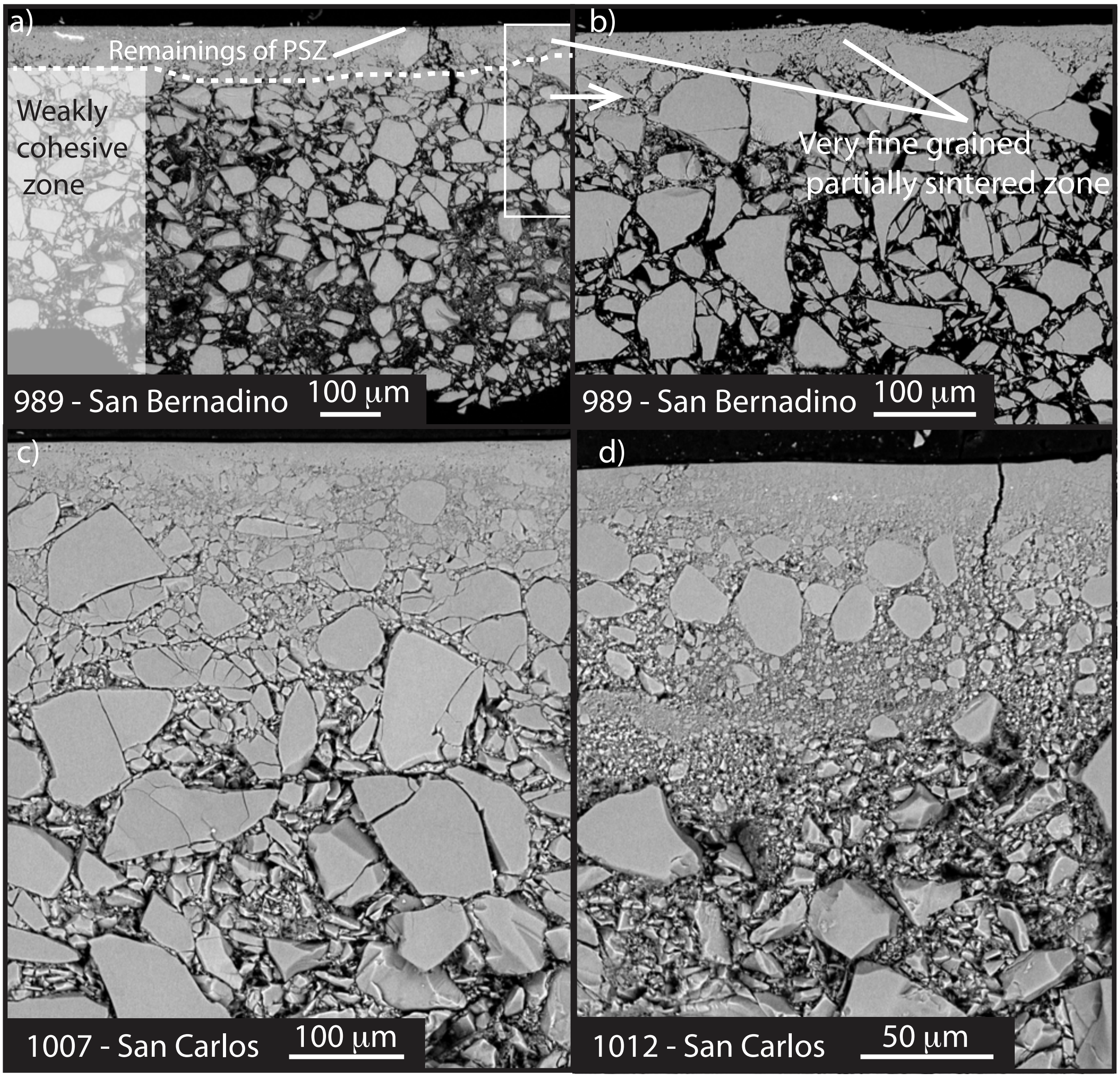

Fig. 8. SEM images: (a) and (b) Forward scattered electron images of the deformed San Bernadino olivine 989; (c) Forward scattered electron images of the deformed San Carlos olivine 1007 and (d) 1012. The three samples were deformed at the same velocity (1 m/s), but have different final slip (0.94 m of slip for 989, 0.97 m of slip for 1007 and 0.07 m of slip for 1012).

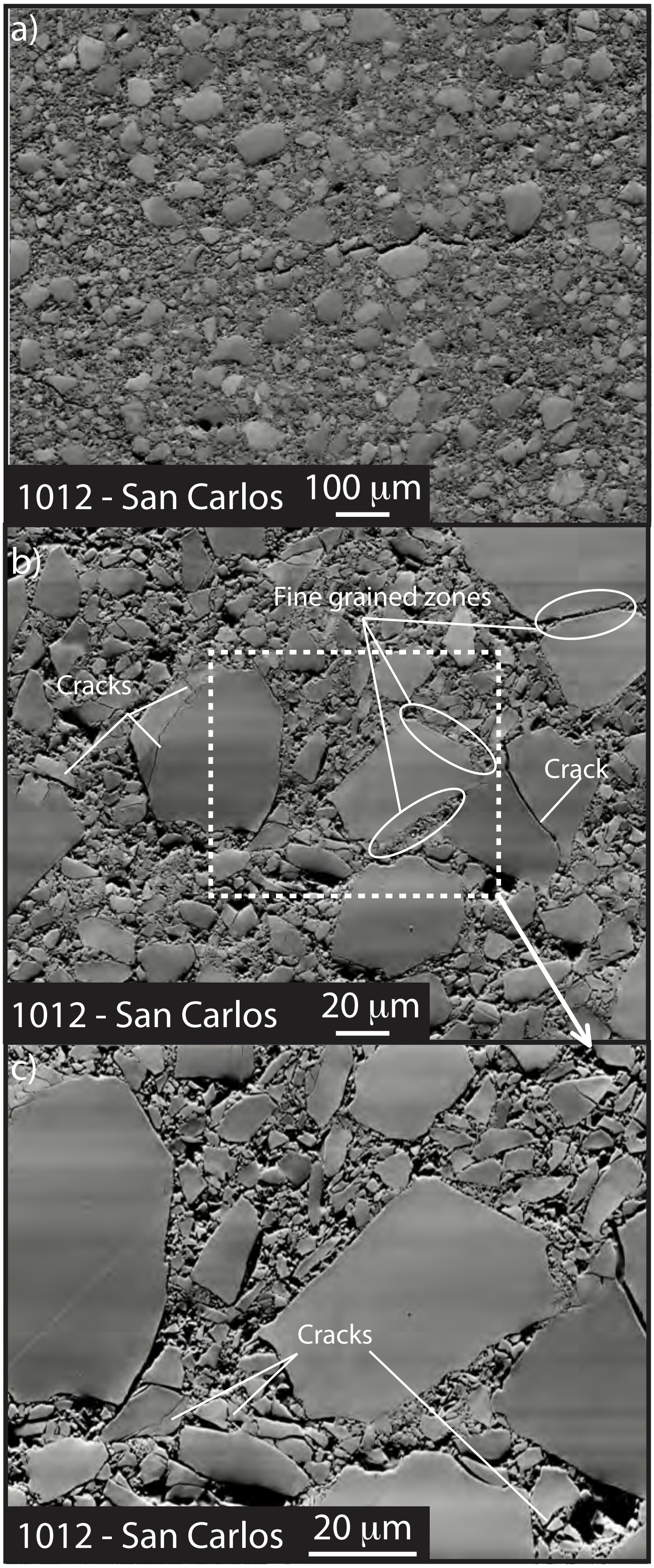

Fig. 9. SEM images: Forward scattered electron image from near the finest grain zone in San Carlos olivine 1012 (1 m/s and 0.07 m of slip) with increasing magnification. The horizontal lines in (b) and (c) are scanning artifacts linked to holes.

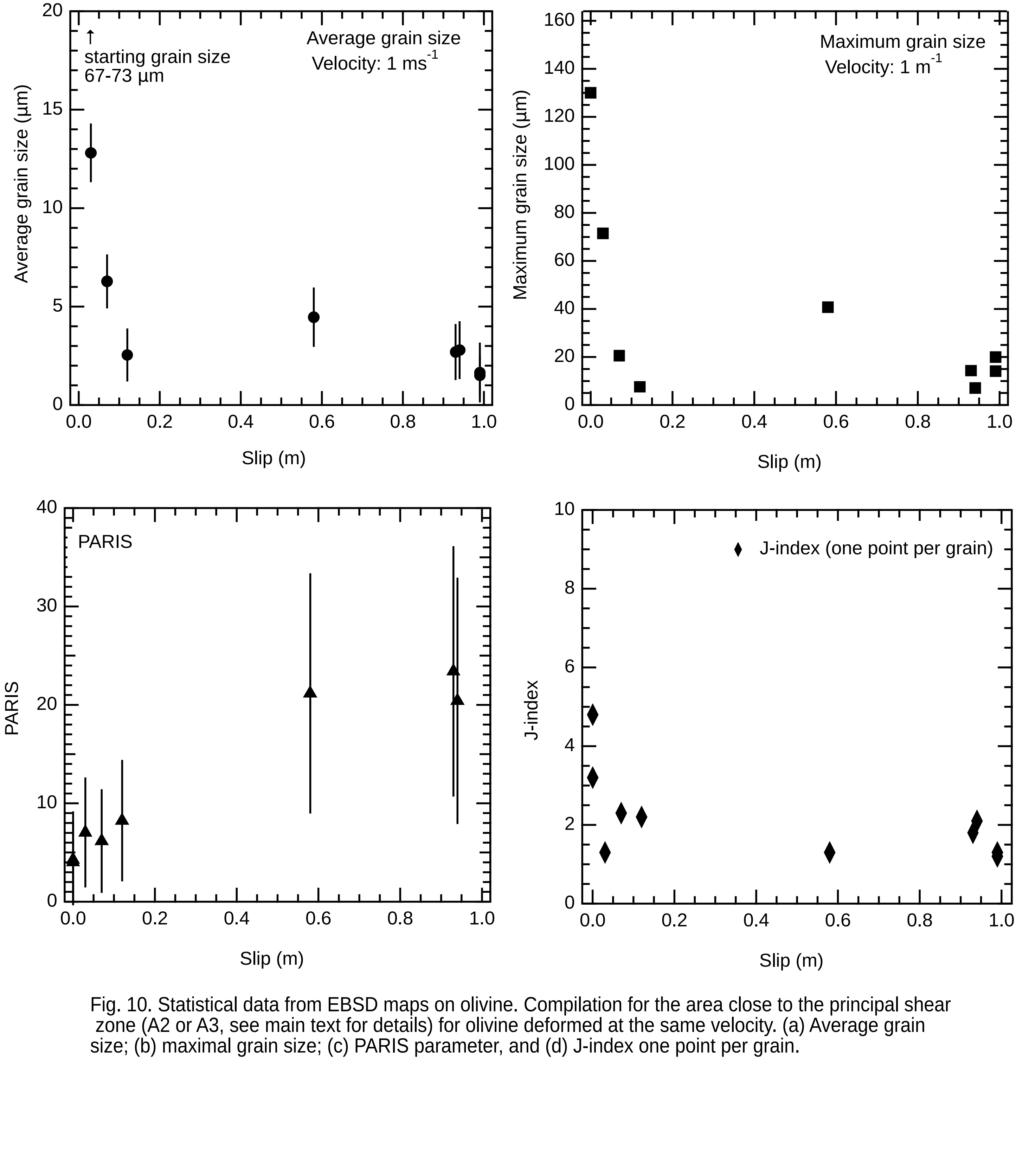

Fig. 10. Statistical data from EBSD maps on olivine. Compilation for the area close to the principal shear zone (A2 or A3, see main text for details) for olivine deformed at the same velocity. (a) Average grain size; (b) maximal grain size; (c) PARIS parameter, and (d) J-index one point per grain.

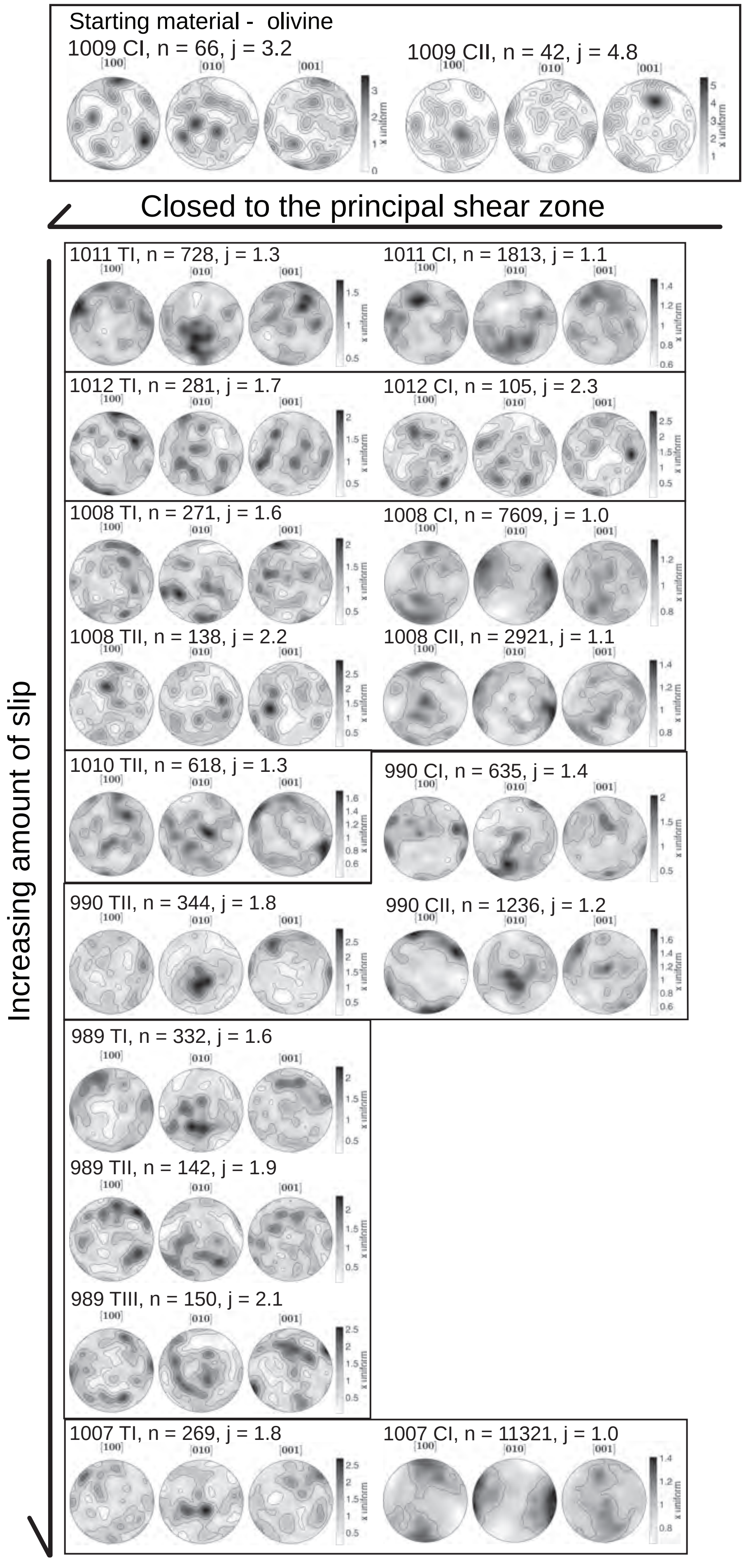

Fig. 11. Pole figures for olivine samples: Lack of well defined crystallographic preferred orientation in olivine aggregates in a lower hemisphere equal-area projection (see Table 2 for details). N indicates the number of grain and j stands for J-index (see methos section for details).

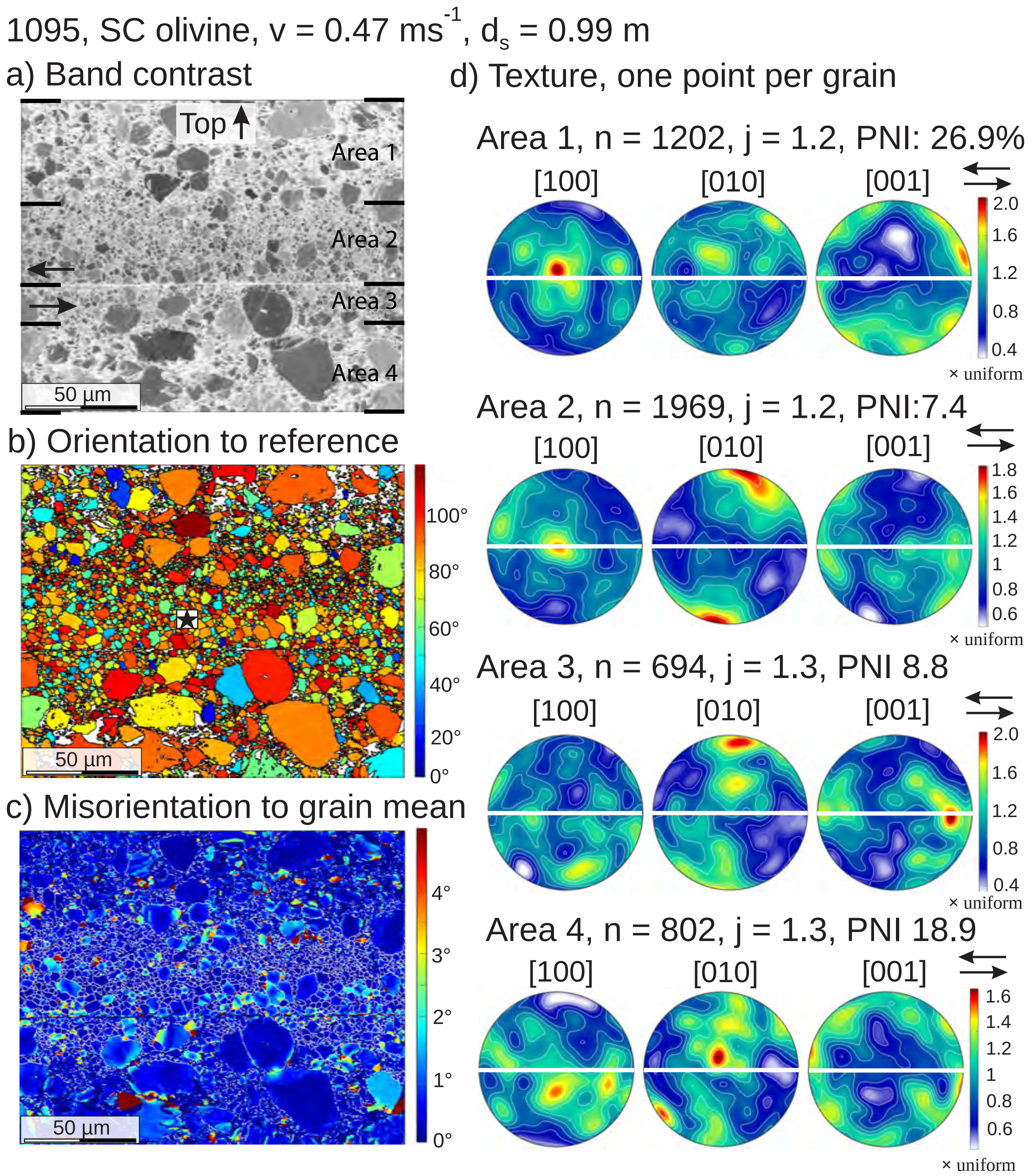

Fig. 12. Microstructure characterization of sample 1095: (a) band contrast image ; (b) crystallographic misorientation to a reference point (i.e., map center, marked with a black star) ; (c) Misorientation to the mean of each respective grain (Mis2Mean, see main text for details); and (d) pole figures of texture for sample 1095, deformed at 0.47 ms-1 and a slip of 0.99 m for each area (A1 to A4) marked in (a). The pole figures of texture and J-index have been calculated using the mean orientation of each grain. Note that area A1 is located outside and at the top of the principal shear zone (PSZ), area A2 and A3 represent both sides of the PSZ, on each side of the mirror surface, and area A4 is located outside and at the bottom of the PSZ. The number of grains considered for each pole figure is given by n, the percentage of non-indexed pixel (a proxy for porosity) given by PNI. Note in (c) the presence of a few abnormal grains and grain portions with high misorientation (<15), which do not impact the CPO results.

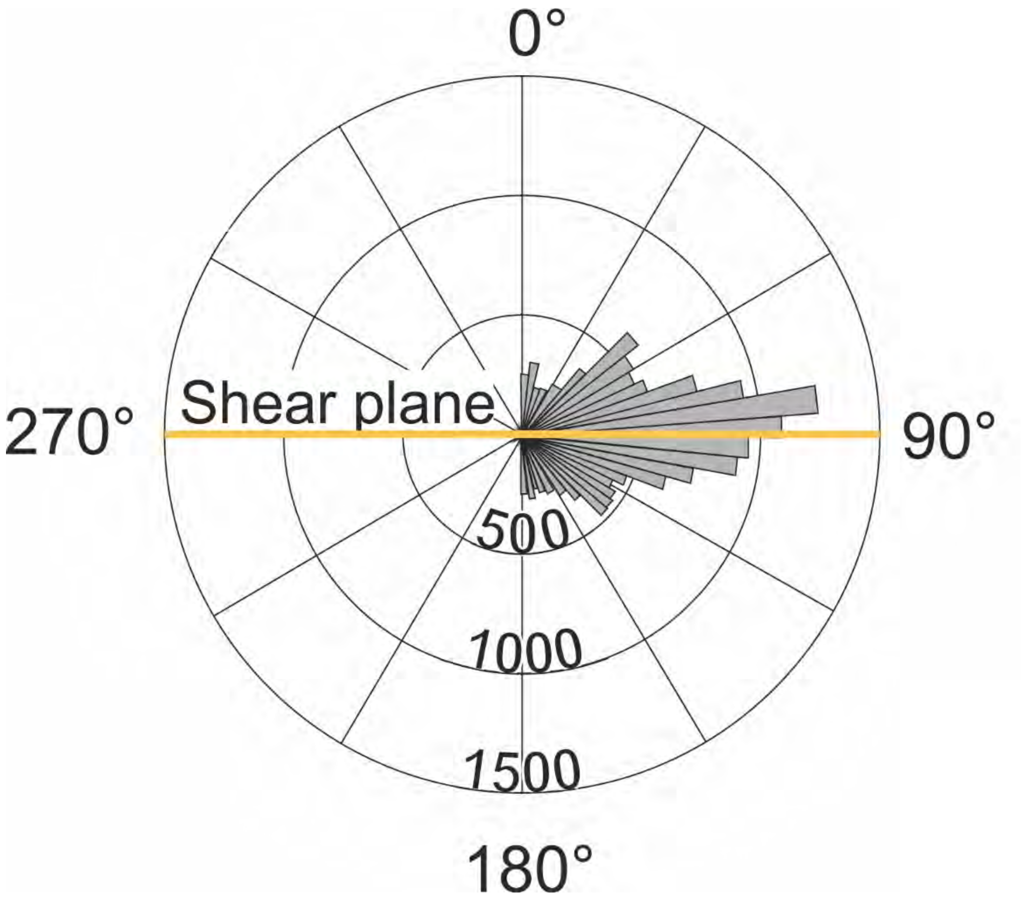

Fig. 13. Rose diagram: the orientation of the long axis of the olivine grains relative to the shear plane. The sample of San Carlos olivine (1007) was deformed at 1 ms^{-1} to 1 m of slip and is representative for all the deformed samples of this study.

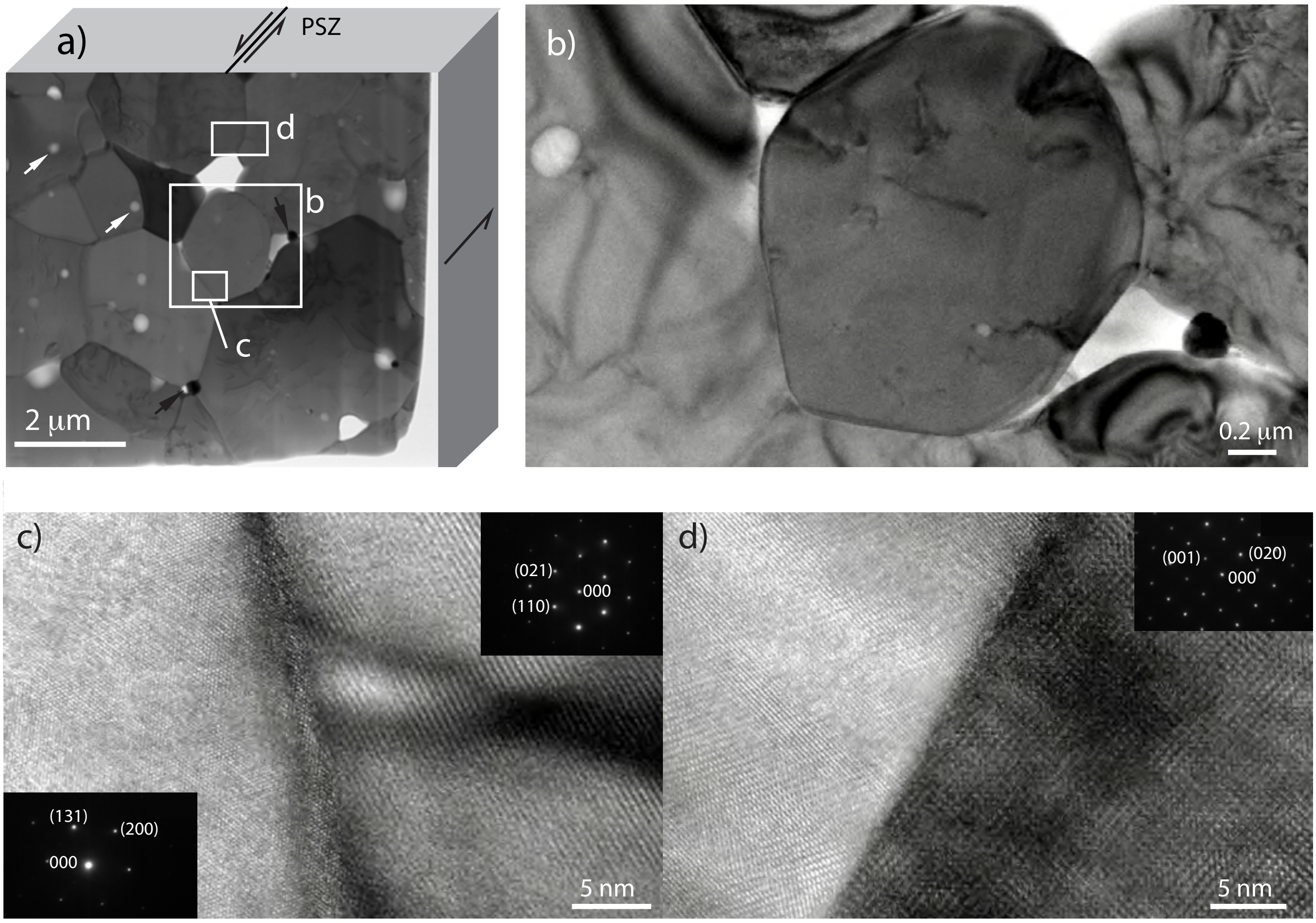

Fig. 14. TEM images: Section inside and perpendicular to the principal shear zone (PSZ) of sample 1095. (a) 3D sketch showing the full focus ion beam section and its orientation towards the PSZ and shear direction. White boxes give the position of the subsequence images (b), (c) and (d). White arrows indicate nano-bubbles, black arrows indicate nano size grains at triple junctions. (b) Zoom into the center grain showing few dislocations. (c, d) High resolution TEM images showing melt-free grain boundaries. Note the absence of intragranular cracks, the remaining porosity, the well-sealed and melt-free boundaries, and thus the partial sintering of the PSZ. Intragranular nanobubbles are common in San Carlos olivines (see Mosenfelder et al., 2011; Burnard et al., 2015).

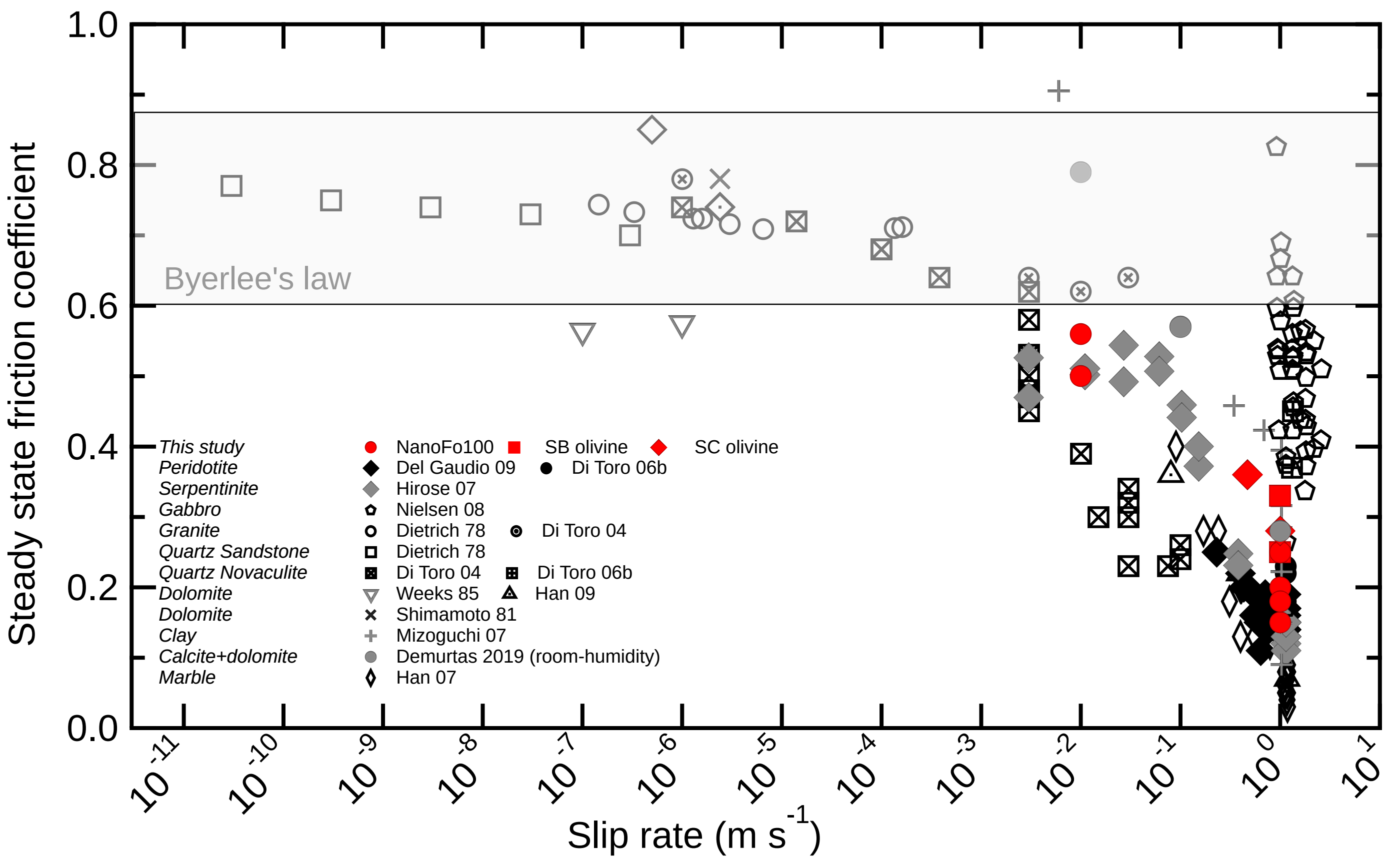

Fig. 15 Evolution of friction coefficient as a function of log slip rate. Red symbols represent olivine aggregates from this study. Data from Dietrich et al. (1978), Shimamoto and Logan (1981), Weeks and Tullis (1985), Di Toro et al. (2004), Di Toro et al. (2006b), Han et al. (2007), Hirose and Bystricky (2007), Mizoguchi et al. (2007), Nielsen et al. (2008), Del Gaudio et al. (2009), Han (2010) and Demurtas et al., (2019).

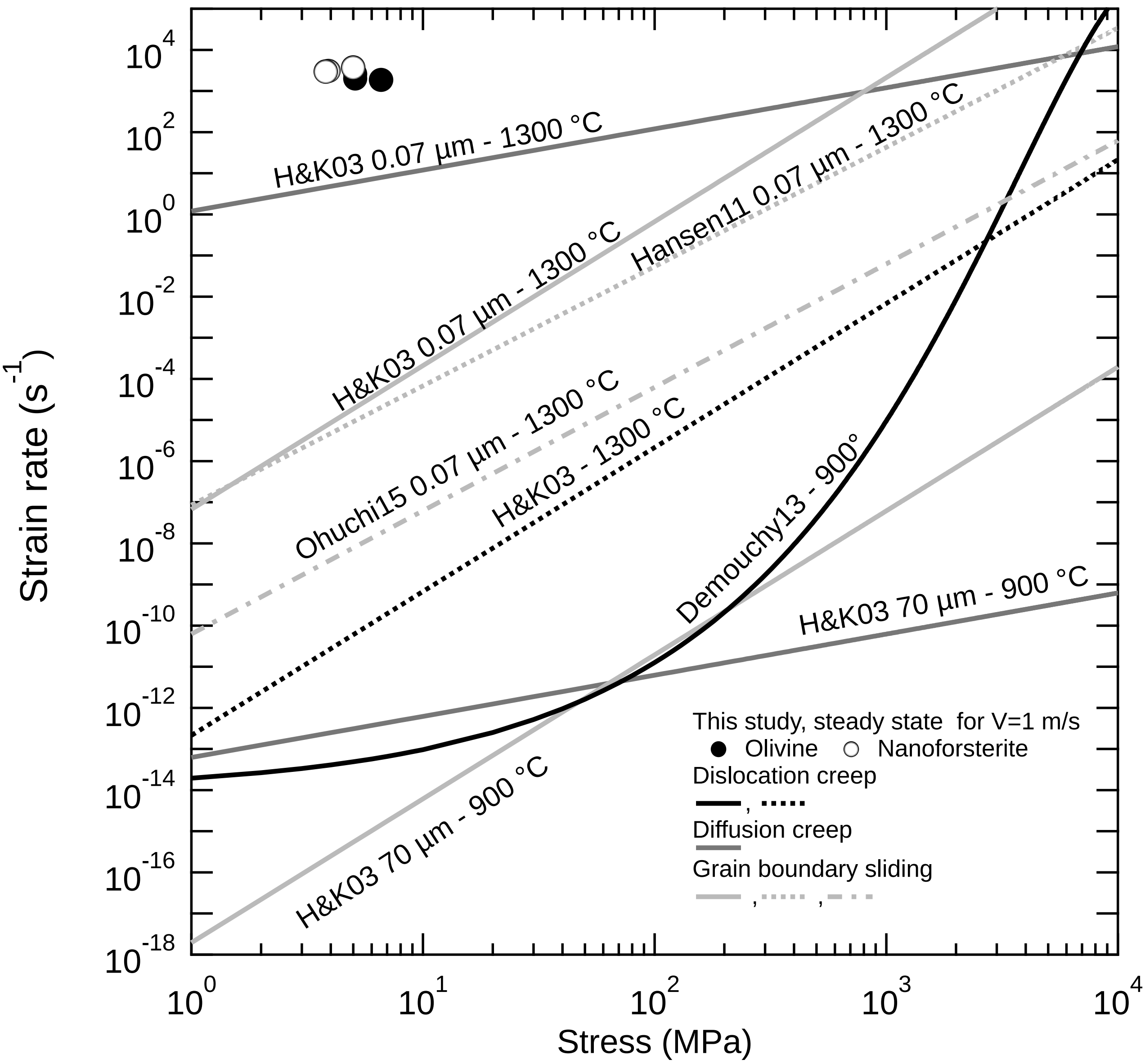

Fig. 16. Strain rate – Stress space. Comparison between the results from this study (steady state values from olivine and nanoFo100) and experimentally established flow laws for low temperature dislocation creep (Demouchy et al., 2013), high temperature dislocation creep (Hirth and Kohlstedt, 2003), diffusion creep (Hirth and Kohlstedt, 2003 for two different grain size and high and low temperature), and finally grain boundary sliding (Hirth and Kohlstedt, 2003; Hansen et al., 2011 and Ohuchi et al., 2015, for 1300 °C and fine grain size).

Shear deformation of nano- and micro-crystalline olivine at seismic slip rates

Manuel Thieme[1], Giacomo Pozzi[2§], Sylvie Demouchy[1*], Nicola De Paola[2], Fabrice Barou[1], Sanae Koizumi[3], Budhika Mendis[4], Leon Bowen[4]

1 Geosciences Montpellier, CNRS & Université de Montpellier, UMR 5243, 34095 Montpellier, France

2 Department of Earth Sciences, Rock Mechanics Laboratory, Durham University, Durham, DH1 3LE, UK

3 Earthquake Research Institute, University of Tokyo, 1-1-1 Yayoi, Tokyo, Japan

4 Department of Physics, Durham University, Durham, DH1 3LE, UK

§ now at Istituto Nazionale di Geofisica e Vulcanologia Via di Vigna Murata 605, 00143 Roma, Italy

Supplementary Materials

Figure S1: SEM image prior to Energy Dispersive Spectrometry (EDS) measurements on the San Bernardino olivine (run # 989).

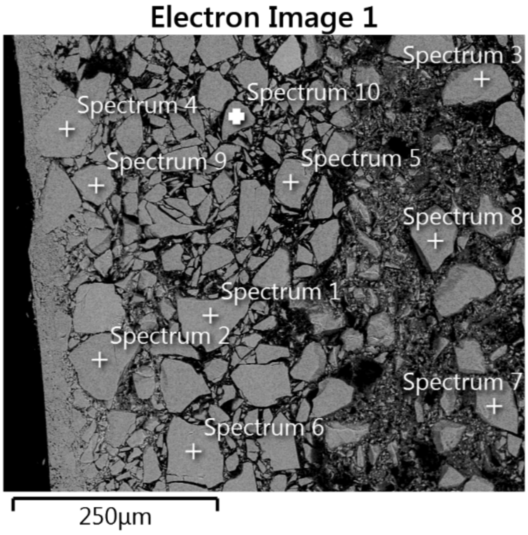

Table S1 EDS measurements on the San Bernardino olivine (run # 989).

Weight %	C	O	Mg	Si	Ti	Fe	Total
Average (N=10)	10.47	54.58	19.98	11.14	0.02	4.53	100.1
1 std dev.	0.49	0.54	0.56	0.32	0.03	0.08	
Normalized without C		72.8	16.9	8.47	0.12	1.73	100
Atom per formula unit		4	1.899	0.953	0	0.194	**Fo = 90.71**

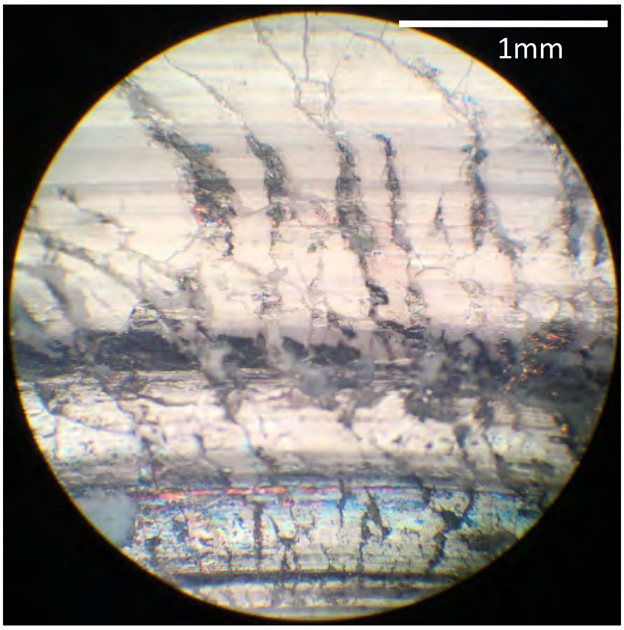

Figure S2: Sample 992 with Riedel shear-like features.

Fig. S3, Thieme et al.

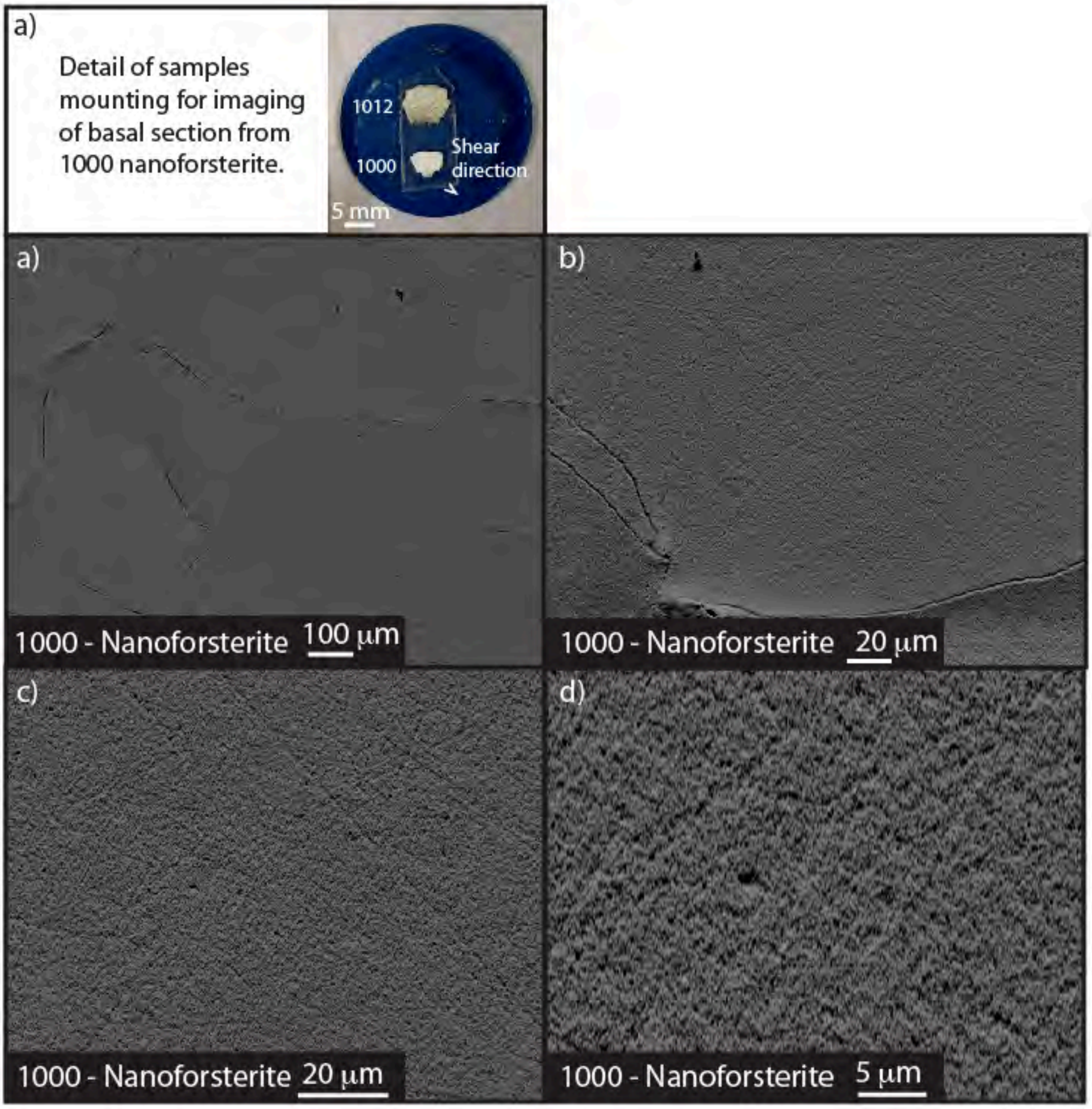

Figure S3: SEM (electron forward scatter) images of nanoforsterite samples post-deformation, illustrating the difficulties of polishing of this type of sample.

Fig. S4, Thieme et al.

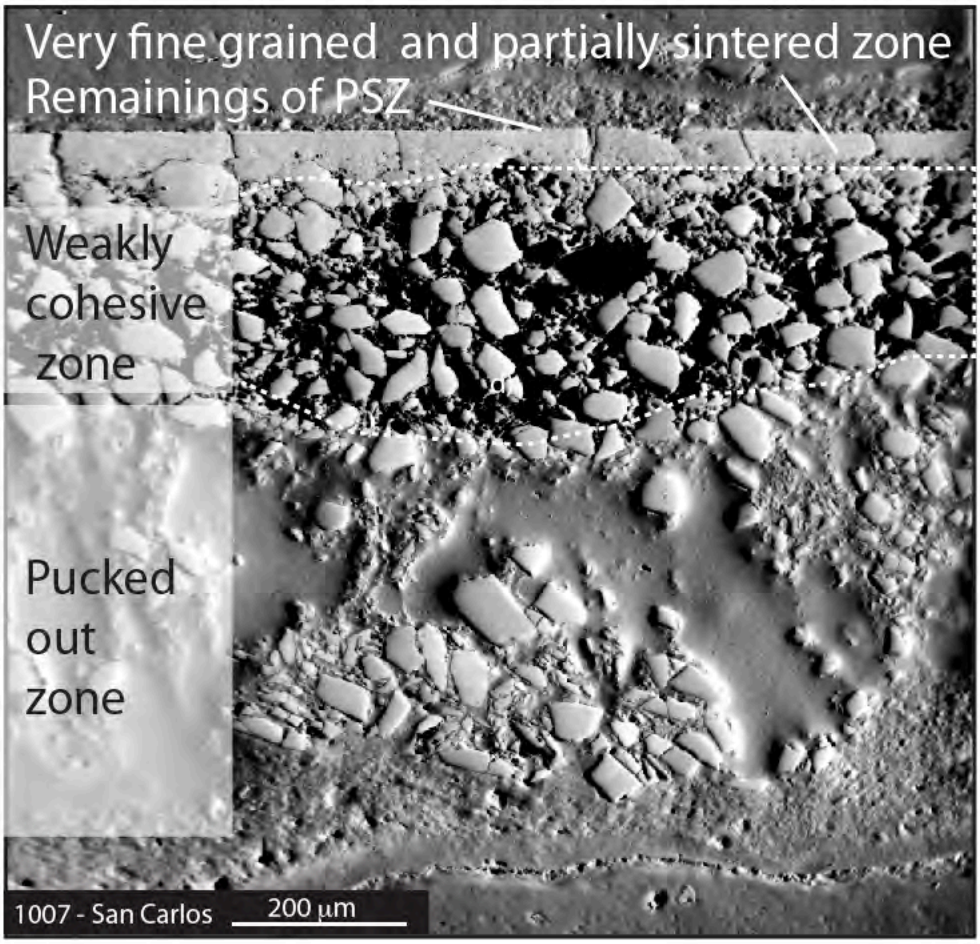

Figure S4: SEM (electron forward scatter) images of San Carlos olivine 1007 post-deformation, illustrating porosity and challenging sample preparation.